A Viscoelasticity Evaluating System of Amyloid-β Peptide Fibrillation on Electrodeless Quartz Crystal Microbalance Biosensor

Yen-Ting Lai

SEPTEMBER, 2018

A Viscoelasticity Evaluating System of Amyloid-β Peptide Fibrillation on Electrodeless Quartz Crystal Microbalance Biosensor

A dissertation submitted to
THE GRADUATE SCHOOL OF ENGINEERING SCIENCE
OSAKA UNIVERSITY

in partial fulfillment of the requirements for the degree of
DOCTOR OF PHILOSOPHY IN ENGINEERING

BY

Yen-Ting Lai

SEPTEMBER, 2018

Abstract

Alzheimer's disease, one of the most devastating dementia, is an elderly suffered illness which involves neurodegenerative disorder. The disease pathogenesis is recently found that it is related to a structural-changing phenomenon: Amyloid β (Aβ) aggregation. In order to clarify the pathogenesis, researchers have made intensive efforts for studying the Aβ aggregation both *in vitro* and *in vivo* (or clinical). However, most of the previous *in vitro* studies were held in bulk solutions and which are different from the process in reality, where the aggregations take place on the cell membrane. In the present thesis, the aim is to develop an *in vitro* Aβ aggregation detection system on a surface, which more resembles to the *in vivo* Aβ aggregation, and to analyze the aggregation process from mechanical viewpoint.

The measurement is based on an electrodeless quartz-crystal-microbalance (QCM) biosensor. Here, Aβ aggregations is taken place on surfaces of the quartz crystal, which is similar to those of the actual Alzheimer's disease. Since sizes of amorphous-like Aβ aggregates were reported to be about 100 nm or less, a nanoscale sensing QCM should be established. To this end, a high frequency quartz crystal, whose fundamental resonant frequency is 58 MHz, is used and the resonance overtones up to 7^{th} modes is measured simultaneously. The quartz crystal is sealed in a package which is equipped with a small chamber to hold the quartz lightly in preventing energy loss by attachment. By connecting a microchannel embedded in the package, Aβ monomer solution can be introduced to the quartz crystal. Consequently, the aggregation can be monitored *via* acoustic overtones of QCM. Present experimental studies revealed that the overtone frequencies are shifted as progress of the Aβ aggregation, and that the aggregation process is classified into three stages. First is the binding stage where the frequencies have dropped as soon as the solution is injected. Second is the lag stage where frequencies are relatively stable for a long time after the binding stage. Finally, we have noticed the frequency ramp stage, where increasing in frequencies are found after the lag stage at around 20 hours.

In order to analyze the experimental results obtained by QCM, a two-dimensional viscoelastic model is introduced. It is consisted of three acoustic layers including quartz crystal, viscoelastic Aβ and surrounding liquid. This model relates the acoustic overtone frequencies to mechanical properties of Aβ aggregates on the quartz surface, *i.e.*, shear stiffness, viscosity, and thickness. This analysis revealed that the mechanical properties change with the stages in frequency response. In the binding stage, the three properties, shear stiffness, viscosity, and thickness, increased simultaneously due to the growth of the viscoelastic layer of Aβ. In the lag stage, the thickness decreases while other properties remained stable. It indicates that condensation of the monomers to Aβ aggregates are taken place on the QCM surface. In the frequency ramp stage, the

stiffness increases with decreasing of thickness. In this stage, we have found the transformation of amorphous-like Aβ aggregates into the crystal-like fibrils.

In addition to the above mentioned QCM measurements, we conducted another observation of morphology of Aβ aggregates formed on the QCM by atomic force microscopy (AFM). In this experiment, QCM monitoring are interrupted in a pre-assigned stage and the surface of QCM is observed by AFM to clarify the relation between the mechanical properties and morphologies of Aβ. After the binding stage, small Aβ aggregates are confirmed on the surface of QCM. The aggregates are consisting of Aβ monomers and which cause the increasing in the three properties. After the lag stage, we confirmed the growth of the aggregates due to condensation and finally, after the frequency ramp stage, the rod-like fibrils, *i.e.*, fibrillation is verified. From the experimental and theoretical analysis, we conclude that the present viscoelasticity evaluation system can detect the sequential structural change of Aβ aggregates on QCM surfaces. Consequently, the thesis revealed the mechanical properties of Aβ in entire aggregation process. The system has promising usage in further applications such as discovering inhibitory medicines in drug development.

Table of content

Chapter 1. Introduction 1

1-1. Alzheimer's Disease and the Diagnosis of Amyloid β 1

1-2. Quartz Crystal Microbalance 2

1-3. QCM Biosensor and Amyloid β 3

1-4. Mission and Objective 4

Chapter 2. Amyloid β Peptide 6

2-1. Amyloid β Peptide (Aβ) and Their Formation 6

2-2. Amyloid β Aggregation 7

Chapter 3. QCM Biosensor 9

3-1. Quartz Crystal Microbalance 9

3-1-1. Resonance frequency and thickness shear mode of QCM 9

3-1-2. Euler angle of crystal and AT-cut quartz 12

3-2. Electrodeless-QCM Biosensor 14

3-2-1. Wireless vibration 14

3-2-2. Amyloid β sensor and sensing system 15

3-3. MEMS QCM Biosensor 16

3-3-1. The introduction of MEMS packaged WE QCM 16

3-3-2. Fabrication of MEMS QCM 18

Chapter 4. Viscoelastic Model of Amyloid β QCM Sensor 21

4-1. Viscoelasticity 21

4-2. MEMS QCM and Viscoelastic Evaluation 23

4-3. 3-layer Model and Inverse Calculation 24

Chapter 5. Frequency Response and Surface Analysis of Amyloid β Aggregation 29

5-1. Solution Preparation 29

5-1-1. $A\beta_{1-42}$ seed solution 29

5-1-2. $A\beta_{1-40}$ monomer solution 29

5-2. Overtone Experiments 30
5-2-1. Preparation of MEMS QCM biosensor 30
5-2-2. Experiment procedure 32
5-2-3. Result 33
5-3. Correlation Experiment 34
5-3-1. Preparation of WE-QCM biosensor without package 34
5-3-2. Experiment procedure 35
5-3-3. Atomic force microscope observation 36
5-3-4. Result 36
Chapter 6. Viscoelastic Analysis and Discussion 39
6-1. Correlation of Viscoelastic Responses to Surface Transition 39
6-2. Reproducibility of Viscoelastic Response During Fibril Transition 41
Chapter 7. Conclusion and Future Prospective 46
7-1. Conclusion 46
7-2. Future Prospective 46
References 48

Chapter 1. Introduction

1-1. Alzheimer's Disease and the Diagnosis of Amyloid β

Alzheimer's disease (AD) is a neurodegenerative disorder characterized as one of the most frequent causes of senile dementia [1]. The irreversible disease made 46 million people suffer and the number is expected to reach 131 million by 2050 worldwide [2]. Synaptic loss and neuronal death that occur in AD brain were found in cerebral cortex, entorhinal cortex, and hippocampus and were said to cause cognitive dysfunction [3, 4]. This neurodegeneration is responsible for the disease to slowly consume the patients of their memories, personalities, ability to perform daily activities, and eventually their lives [5]. Therefore, understanding the pathophysiological mechanisms and the kinetics underlying neurodegeneration is essential for the rational design of therapies that will slow down or halt the disease progression.

The disease is considered "senile" or "elderliness" because age is the most significant risk factor for the on-set chance of disease, which doubles every 5 years after 65 [6]. However, the disease can also strike earlier and is called early-onset AD, which develops in the age group of 45-64. Fortunately, the early-onset AD has a low incidence of 4.2 out of 100,000 people [7]. The cognitive and pathological changes about on-set of the disease are highly similar, and all cases were identified to converge on the process of the altered amyloid precursor protein (APP) [8].

AD first became recognizable at the 1960s, when M. Kidd and R. Terry successfully described the structural changes in senile plaques and fibrillated neuro tangles by electron microscopy at the same time [1]. The AD was then generally accepted as the most common cause for senile dementia in the late 1960s [9]. In the same decade, the pathogenesis of AD was also discovered to associate with amyloidosis, which is the fibrillous Amyloid Beta (Ab) plaque found in the brain of AD patients. By involving chromatography (Sephadex G-100), the plaque was identified as the precursor of no homology [10]. In the 1980s, AD became distinguishable from other dementia, where it did not involve degeneration of just homogeneous but highly heterogeneous transmitting neurons (or synaptic) [11]. Attention increasingly focuses on identifying the mechanisms for the malfunction and degeneration that affect multiple classes of neurons in the limbic system and associated cortices. Although the vascular amyloidosis was revealed by Fischer in early 1900s [12], the relationship between the Ab to AD was not linked-up until the 1980s. From then on, a wide variety of studies have focused on clarification of the Ab characteristics [13] and the mechanism of Ab structural transition [14]. Other incurable dementias are listed in Table I with their proteins which causes the pathogenesis.

Table I Typical dementia and featured protein in body part.

Disease	Featured protein and relative residues	Degenerative disorder region
Alzheimer's disease	Amyloid-β, 40-42 [1, 4, 6]	Brain, hippocampus in most cases
Parkinson disease	α-synuclein [6, 15]	Central nervous system
Dialysis-related amyloidosis	β2-microglobulin [16]	In bone
Prion disease	Prion protein [17]	Brain
Huntington's disease	Huntingtin [18]	Brain

1-2. Quartz Crystal Microbalance

Nowadays, acoustic wave devices are widely applied as sensors, actuators, frequency references and in wireless communication systems. In the application of sensor, bulk acoustic wave (BAW) device is one of the most commonly used devices in many fields of sensing technology because of the advantages in integrated dimension well sensitivity in mass detection and frequency stability. Among the BAW sensors, Quartz Crystal Microbalance (QCM), made of a quartz resonator, shows the most competitive [19, 20].

A quartz resonator refers to a device based on a quartz plate or film with two electrodes embedded on each surface which can be excited piezoelectrically when exerting with alternative electric signals. Piezoelectric effect is an intrinsic behavior of materials such as quartz, which is described as the coupling effect where the transition between electrical energy and the mechanical energy occurs. It was first discovered by Pierre Curie and Jacques Curie in 1880 and was first used in practically during World War I where Langevin et al. developed an ultrasonic submarine detector with a transducer made of thin quartz crystals glued between two steel plates [21]. It was 1959 when Sauerbrey demonstrated this phenomenon with quartz crystal [22] and established the Sauerbrey equation based on the linear relationship between resonance frequency and surface mass variation of quartz, and the first to declare the name quartz crystal microbalance (QCM) because of the sensitivity to micro and nano-scale material attached to the quartz surface.

Sauerbrey equation is valid for elastic subjects such as metallic coatings [23], metal oxides [24], and thin adsorbed layers, where these materials owe high rigidity and merely dissipate any energy during oscillation. However, the Sauerbrey equation does not work on soft and viscous materials such as cells, polymers, and biomolecules, where energy loss appears due to viscous damping, making the equation inaccurate.

The linear relationship between resonance frequency and surface mass would also collapse when the mass change on QCM is greater than 2% of the quartz crystal mass [25].

Aside from the Sauerbrey equation, Kanazawa et al. found that the QCM was still available in evaluating viscous-material from Helmholtz equation [26]. This makes the QCM more adaptive, and hence provides a wide variety of sensing applications, including immunoassay [27, 28], liquid phase properties [29, 30], and gas phase properties [31-34]. In addition, researchers have developed different configuration QCM to satisfy different circumstances, such as:

1. QCM with dissipation, QCN-D: measuring QCM resonance frequency with the resonant intensity, simultaneously for more precise determination of the viscous damping materials from intensity dissipation of QCM [35, 36].
2. Surface contour: trapping the vibration energy inside QCM from leaking into the mechanical support of QCM, which includes bi-convex and edge beveled quartz [37, 38].
3. Modifying electrode topologies: improving the sensitivity of QCM by removing the electrode from the sensing surface of QCM, including:
    a. Lateral field excitation (LFE), where electrodes are placed on the opposite side of the sensing surface [39, 40].
    b. Wireless-electrodeless QCM (WE-QCM), where electrodes are completely removed from the quartz surface, leaving both surfaces of the quartz chip for sensing [41-43].

1-3. QCM Biosensor and Amyloid β

A biosensor is an innovative analytical device which possesses biological recognition, including a wide range of applications such as drug discovery [44], diagnosis [45], biomedicine [46], food safety and processing, and environmental monitoring [47]. The general methodology of a biosensor is to detect the physical property of bio-interaction such as surface mass change caused by molecule affinity in QCM. The surface mass change is then coupled with electrical signal and is read by electronic devices which have a visible interface such as PC. The first biosensor ever reported was the invention of Clark and Lyons, which was an enzyme-based biosensor where electrodes were coupled with enzyme catalysis electrochemically to measure blood glucose in biological samples in surgery assistance [48]. Other biosensors include cytosensor microphysiometer: based on cellular systems [49], spectrophotometric: where targets were observed with the assistance of fluorescence [50], quartz crystal microbalance (QCM) [28, 43] and surface plasmon resonance [51]: which are biologically immobilizing-based components, and *etc*. Among the various types of biosensors, QCM is profitable because of simple, cost-effective, high-resolution in

mass sensing, and which can function as a label-free biosensor. In the 1980s, liquid solution based QCM sensor was developed as new technology advancing that measured frequency change from QCM could be related to changes in viscosity and density in liquid media where highly damping should be considered [52, 53]. The relation between QCM frequency change to liquid viscosity and density is then described mathematically by Kanazawa *et al*. [25, 26].

Recently, a QCM with wireless and electrodeless configuration has been promoted by Ogi *et al*. [41] by isolating the electrodes from the quartz resonator. With the electric field penetrating through the quartz crystal via a medium (target solution), the quartz chip can still be excited [54, 55]. This configuration greatly improves the quality factor of QCM from the possible damping caused by metallic electrodes and also the sensitivity to smaller targets (like Aβ monomers).

Although the aggregation phenomenon of the Aβ peptides has been studied for decades, the reaction was usually performed in bulk liquids [56-58], where critical problems always arose: The Aβ aggregation reaction in bulk solution proceeds with many interactions among different aggregates (monomer, oligomers, and fibrils). This could cause the aggregate products different from the amyloid plague formed on the surface of cell membrane. Because the aggregation reaction *in vivo* proceeds on membrane surface where only Aβ monomers are deposited on the Aβ nuclei, it is preferable to study the aggregation reaction on the surface *in vitro* as well, not in the bulk solution.

It has been shown that $A\beta_{1-42}$ seeds immobilized on surface capture $A\beta_{1-40}$ monomers, resulting in oligomeric layers [59, 60]. This binding system is practically important for two reasons. First, $A\beta_{1-42}$ peptides show much higher hydrophobicity than $A\beta_{1-40}$ [61] and they easily form the aggregation nuclei on the membrane surface. Second, the number of $A\beta_{1-40}$ are the highest in human brain [62-64], and they will accumulate on the $A\beta_{1-42}$ seeds. Therefore, the binding of $A\beta_{1-40}$ monomers to the surface not only realize the similar phenomenon in *in vivo*, but also fulfill the need of monitoring the QCM signal for life-long aggregation of the Aβ.

1-4. Mission and Objective

The goal of this study is to develop a diagnosis system of the Aβ aggregation for future assistance in search of solutions to the AD. Therefore, we established an Aβ aggregation evaluating system which is based on wireless-electrodeless QCM and monitored the QCM signal for the life-long incubation of $A\beta_{1-40}$ peptide from monomer deposition to the dead end of structure transition (into fibril). The QCM chip is packaged in silicon microchannel, and the frequency responses were monitored in real-time, up to the 7^{th} overtones. The fundamental resonance frequency of our QCM is about 58 MHz so that the 7^{th} mode exceeds 400 MHz. This very-high-frequency QCM

improves the mass sensitivity for smaller particles like $A\beta_{1-40}$ (molecular weight: 4.5 kDa) and allows us to calculate the viscoelastic properties, including thickness, viscosity, and shear stiffness of the Aβ during the aggregation, simultaneously. Note that fundamental resonance frequencies of commercially available QCMs are typically 5-10 MHz [35, 36, 39, 40].

Beside the overtone measurements, we performed the aggregation reaction on a naked QCM, without packaging, to study the correlation between the viscoelasticity change and the surface morphology with atomic-force microscopy (AFM). We succeed in detecting, for the first time, the stiffening phenomenon in the Aβ layer after a long lag time on the surface. And we reveal that this stiffening is caused by the structure transition from oligomers into fibrils.

Chapter 2. Amyloid β Peptide

2-1. Amyloid β Peptide (Aβ) and Their Formation

Aβ is a protein residue (peptide) consisting of 40 or 42 amino-acid sequences as shown in Fig. 2-1. Single-cell Aβ (monomer) is a decomposed component exhibiting mostly in spring-like α-helix secondary structures [65]. This peptide is the result of the precursor protein (Amyloid precursor protein: APP), embedded in the cellular membrane [13]. The Aβ is considered to be neurotoxic through amyloidosis [66], which is commonly known as AD-related neuro-disorder. Normally, α-secretase would snip through APP and a non-neurotoxic fragment, p3, is formed instead of Aβ because α-secretase recognizes a protein sequence closer to the cell surface, which is called a non-pathogenic pathway [67, 68]. But with a very low chance, when sequential cleavage of β-secretase occurs as shown in Fig. 2-2, the Aβ peptide is produced and would aggregate into neurotoxic "plaques" in the brains of AD patients [13, 69].

The numbering 1-40 and 1-42 refers to the amino series. For example, an $A\beta_{1\text{-}40}$ has 40 amino acids in the sequence. The two main sequences exist in a human body denoted by $A\beta_{1\text{-}40}$ (~90%) and $A\beta_{1\text{-}42}$ (~10%) [70] and the series depend on the cleaving position of γ-secretase in the cell membrane as shown in Fig. 2-1.

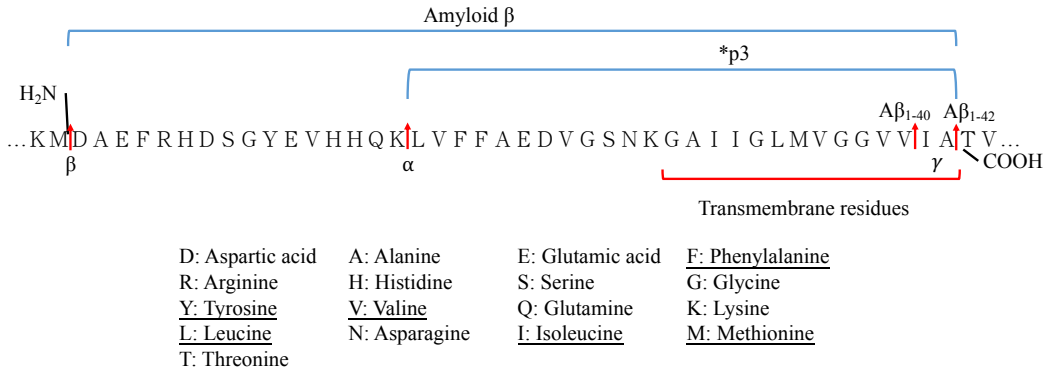

Fig. 2-1 Amino-acid sequence of the amyloidogenic Aβ peptide cleaved from β (left) and γ (right) secretase from the precursor protein, and below show the full names of each amino acids correspond to the letters, where under-line residues indicate the hydrophobic amino acids. *Note that non-Amyloidogenic p3 residue would form if the precursor was cleaved by α secretase, instead of β secretase.

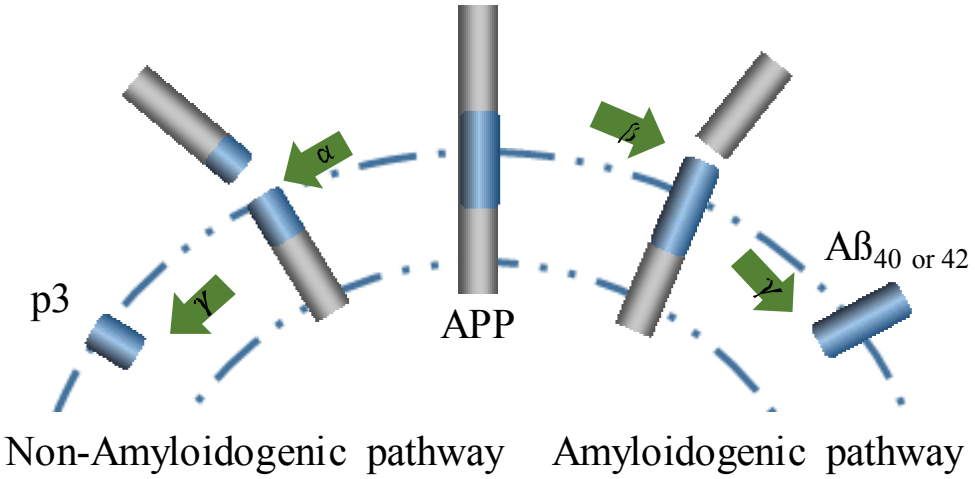

Fig. 2-2 The formation of Amyloidogenic (Aβ) and non-Amyloidogenic (p3) peptide from the amyloid precursor protein (APP).

2-2. Amyloid β Aggregation

The aggregation of Aβ peptides in *in vivo* takes a few years [8, 13] to reach the dead-end amyloid plaques, and it also takes several hours and days *in vitro* experiment [57]. The aggregating Aβ means they owe the self-assembling behavior and form the amyloid fibrils through a specific aggregation pathway, involving oligomer (Fig. 2-3). The Aβ oligomers appear before the fibril state and therefore are called intermediates of the pathway [71, 72].

Oligomers are soluble spherical aggregates and have been studied for many different types of amyloids with TIRF microscopy [60]. These spherical aggregates appear during middle of the pathway and disappear as fibrils appear in dead end, suggesting that they are an intermediate step in the pathway and would transform into fibrils. Their sizes vary depending on the number of monomer aggregates.

The diameter of an Aβ fibril is about 5~10 nm and the fibril structures are characterized by the crossed β-sheet structures (Fig. 2-4) in which the polypeptide chain is oriented perpendicularly to the fiber axis and construct with the hydrogen bond parallel to the axis with the spacing between monomers of 4.7 Å [73]. Both oligomers [74, 75], and fibrils [56, 76] show neurotoxicity, and are recognized as pathogenicity factors for AD. Therefore, clarifying the transition behavior from oligomers into fibrils is not only helpful in understanding the aggregation mechanism (kinetic study of Aβ fibril formation [57, 77, 78]), but also in drug development [58].

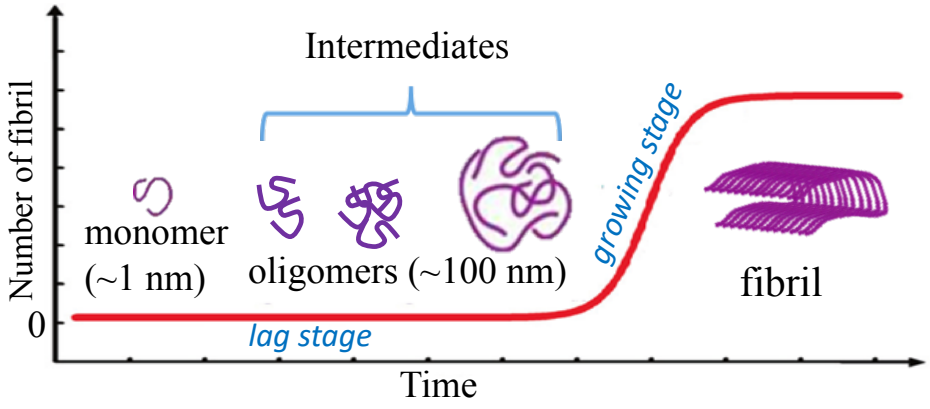

Fig. 2-3 Typical aggregation pathway of the Aβ peptide from the monomer to the fibril dead end.

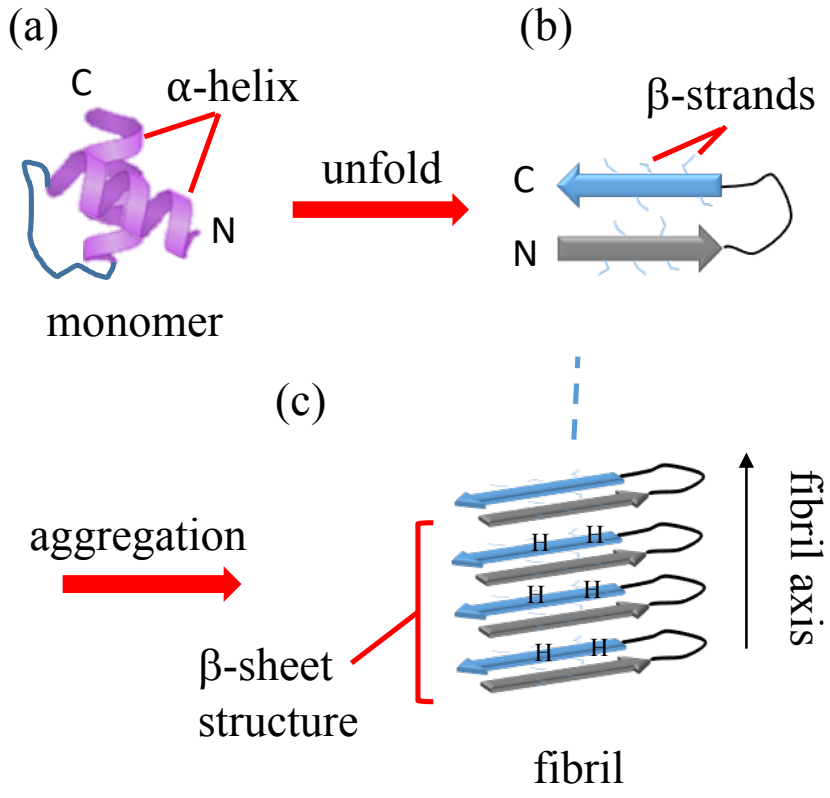

Fig.2-4 Schematic of the general Aβ monomer morphology of (a) α-helix structure with (b) branch-like β-strand stretching outward and (c) β-sheet structure form between monomers of fibrillated Aβ. The gap between Aβ monomer in the cross-β-sheet is about 4.7 Å.

Chapter 3. QCM Biosensor

3-1. Quartz Crystal Microbalance

3-1-1. Resonance frequency and thickness shear mode of QCM

A QCM is a nano-gram-sensitive film-like resonator based on an AT-cut α-quartz crystal. Its resonance characteristic is based-on the piezoelectric effect, which is the coupling between electrical and mechanical energy. By applying alternating voltage, exhibiting the signal as a sine-wave, through the normal axis of the quartz plate, the piezoelectric characteristic of the quartz causes the QCM to deforms in bi-directions, which reveals as a harmonic vibration. When the signal frequency matches the resonance frequency of the quartz, the vibration amplitude becomes the largest and exhibits an intensity peak at the resonance frequency as shown in Fig. 3-1 (a).

The intensity peak is resulted from the deformation pattern (acoustic mode shape) of the quartz crystals during piezoelectric excitation. For a widely used QCM, thickness shear mode (TS mode) is generally measured as the resonance mode of an AT-cut quartz crystal [79]. The mode is characterized by transversal displacement along axial direction where quartz plate deforms in shear direction along the QCM thickness in symmetry to the center line of the quartz plate (Figs. 3-1 (b)-(h)). The fundamental TS mode shape resembles a half wavelength ($\lambda/2$) propagating along the thickness inside QCM as shown in Fig. 3-1 (b). Due to similar characteristic, modes with shorter wavelength resulted in higher resonance frequency, so-called overtone, can also be excited inside the quartz plate.

Among the overtones, the odd modes (Figs. 3-1 (b), (d), (f), and (h)): 3rd, 5th, 7th are detectable, because of the shear displacement on both surfaces are the largest where the deformation is out of phase (180º) in shear direction along the plate thickness. The even modes (Figs. 3-1 (c), (e), and (g)) are undetectable because the shear displacement in even overtones. Take 2nd overtone shown in Fig. 3-1 (c) for example, appears like two reversed shear motions of the fundamental mode in series and would cancel the polarization. Therefore, the resonance frequencies of TS mode can be expressed as

$$f_n = \frac{v_s}{2h_q} n, \tag{3-1}$$

as a result of Figs. 3-1 (b)-(h). Where f_n is the resonance frequency for the nth overtone, v_s is the velocity of the shear wave, which is the square-root of shear modulus divide by mass density of the quartz, h_q is the thickness of the QCM, and n is the overtone numbers, which is normally the odd numbers: 1, 3, 5, 7…….

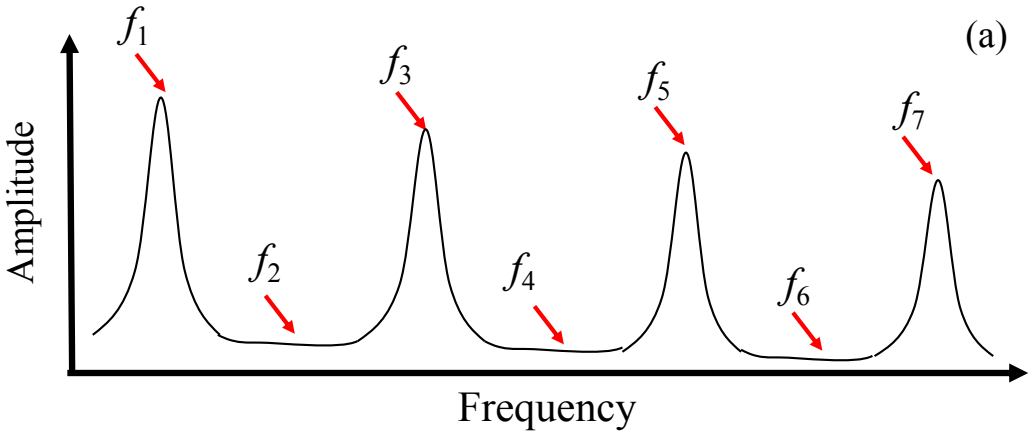

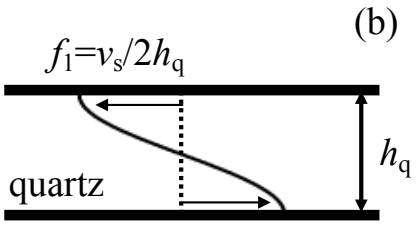

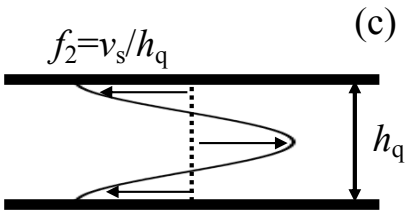

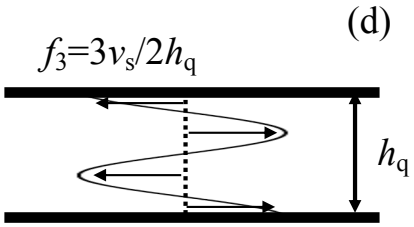

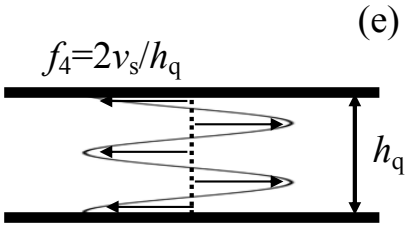

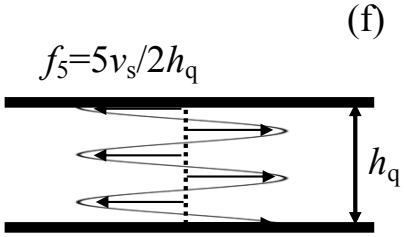

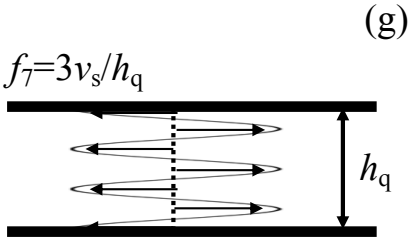

can not be measured

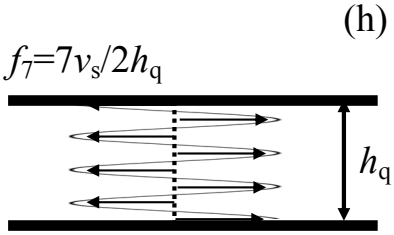

can be measured

Fig. 3-1 Examples of thickness shear (TS) resonance of AT-cut QCM in (a) frequency spectrum of odd overtones (n=1, 3, 5, and 7) that shows resonance peak and even overtones (n=2, 4, and 6) that cannot be detected. (b), (d), (f), and (h) are the TS mode shapes of fundamental mode, 3rd, 5th, and 7th overtone. (c), (e), and (g) are the TS mode shapes of 2nd, 4th, and 6th overtone (even mode) that cannot be detected because the shear distributes along the thickness of QCM is symmetrically resonated, which cancels the polarization. Where arrows in (b)-(h) indicate the shear deformation from the centerline. h_q is the thickness of quartz and v_s is the shear wave velocity propagating inside AT-cut quartz, which is the square root of quartz shear modulus divide by quartz density. Note that the odd modes are measured simultaneously in overtone experiments in this work to proceed the viscoelastic calculation.

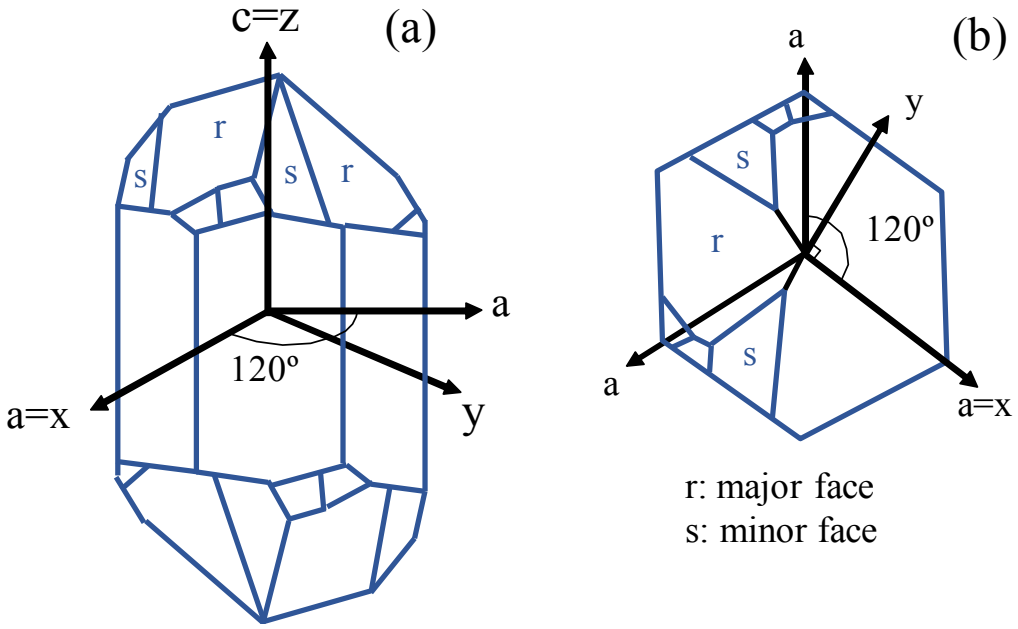

Fig. 3-2 (a) is the α-quartz crystal under orientation of the 1949 IRE standard system and (b) is the top view of the crystal. The imaginary a-axes are lying 120º apart in a plane normal to c-axis.

3-1-2. Euler angle of crystal and AT-cut quartz

Like many other crystals, quartz has a complicated structure of trigonal lattice structure and anisotropy characteristic. The anisotropy results in difference in mechanical properties when measured along different crystallographic axes, where it is important to design the thickness orientation of quartz plate via the angle of crystallographic axis of quartz crystal. This does not only affect the electro-mechanical coupling coefficient, which excites differently when exerting electric field along plate thickness, but also affect the material of its temperature dependencies. Therefore, a different cut angle of quartz crystal will significantly affect the vibration and other material properties such as temperature coefficient [80].

The crystallographic axes are a set of imaginary axes based on the symmetry of the lattices and the crystals. Each crystal system has different customs that define the orientation of the axes. According to the Bravais-Miller axial system, which is most commonly used, there are three equivalent secondary axes (*a*-axes), lying 120º apart in a plane normal to *c*-axis in the α-quartz crystalline system as shown in Figs. 3-2 (a) and (b). By adopting the 1949 IRE crystalline coordinate system, which is widely used in orienting quartz crystal. In the standard, any one of the *a*-axes can be assigned as +*x*-axis and the *c*-axis normal to the *a*-axes plane is generally assigned *z*-axis. Therefore,

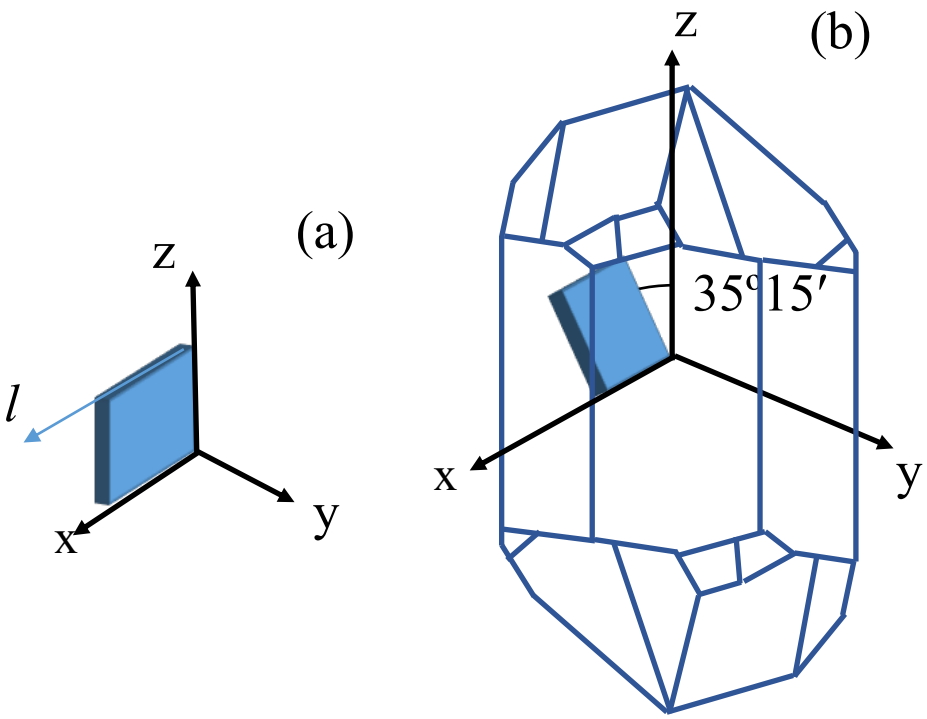

Fig. 3-3 (a) is the axial notation of the plated quartz of 0 degree with *l* indicating the length direction and (b) denotes the cut angle of (YX*l*) 35º15′ also known as the AT-cut with a rotation angle of 35º15′ to the crystallographic *x*-axis.

Table II Names of different angle quartz plate and their mode in use.

Crystal cut	Angle (to *z*-axis)	Excite mode
AT	35º15′	TS mode [29, 30]
BT	-49º	TS mode [81]
ST	42º	Love mode [82]

the imaginary *y*-axis is set normal to the *x*-*z* plane. And this coordination system is defined for the reference of rotation of the quartz plate.

Among all angles, the (YX*l*) 35º15′ cut angle is widely applied because the cut-angle plate generates a clean TS mode, resulting the responded frequency to be stable and a good signal noise ratio (S/N). On the other hand, the frequency-temperature dependency of the quartz under this cut angle is very small under room temperature (<5 ppm/K for 15 to 25ºC) [80]. As the name, this cut angle is 35º15′ (or 35.25º) to the crystallographic *x*-axis which can be seen as the plate rotated 35º15′ to x-axis. The notation (YX*l*) means:

Y: The initial orientation of the thickness direction, which is laid along the *y*-axis.

X: The initial orientation of the length direction, which is aligned with *x*-axis.

l and 35º15′: Rotate 35º15′ about the plate *l*-axis as shown in Fig. 3-3 (a), which is the crystallographic *x*-axis.

The chip under this cut angle is commercially called AT-cut, as shown in Fig. 3-3 (b), which excites a pure TS mode as sorted in table II with other frequently used cut angles and their mode of excitation.

In this work, AT-cut of the pure elastic α-quartz was chosen to perform the experiments. Referring to Euler's transformation of coordinate system, the anisotropic material constants will "rotate" with the coordinate system as if the material constants were observed from different cut angle. For example, the rotation can be expressed in matrix form separately, where

$$\mathbf{R}_{\mathrm{z}} = \begin{bmatrix} \cos\theta_z & \sin\theta_z & 0 \\ -\sin\theta_z & \cos\theta_z & 0 \\ 0 & 0 & 1 \end{bmatrix}, \tag{3-1}$$

$$\mathbf{R}_{\mathrm{x}'} = \begin{bmatrix} 1 & 0 & 0 \\ 0 & \cos\theta_{x'} & \sin\theta_{x'} \\ 0 & -\sin\theta_{x'} & \cos\theta_{x'} \end{bmatrix}, \tag{3-2}$$

and

$$\mathbf{R}_{\mathrm{z}''} = \begin{bmatrix} \cos\theta_{z''} & \sin\theta_{z''} & 0 \\ -\sin\theta_{z''} & \cos\theta_{z''} & 0 \\ 0 & 0 & 1 \end{bmatrix}. \tag{3-3}$$

Where $\theta_z = 0$, $\theta_{x'} = 35°15'$, and $\theta_{z''} = 0$, meaning rotating 0 to original z-axis, 35°15′ to x-axis, and 0 to the new z-axis. With the total rotation matrix

$$\mathbf{R} = [\mathbf{R}_{z''}][\mathbf{R}_{x'}][\mathbf{R}_z] = \begin{bmatrix} R_{11} & R_{12} & R_{13} \\ R_{21} & R_{22} & R_{23} \\ R_{31} & R_{32} & R_{33} \end{bmatrix} \tag{3-4}$$

for 3 x 3 matrix and

$$\mathbf{R}_{6x6} =$$

$$\begin{bmatrix} R_{11}^2 & R_{12}^2 & R_{13}^2 & 2R_{12}R_{13} & 2R_{13}R_{11} & 2R_{11}R_{12} \\ R_{21}^2 & R_{11}^2 & R_{11}^2 & 2R_{22}R_{23} & 2R_{23}R_{21} & 2R_{21}R_{22} \\ R_{31}^2 & R_{11}^2 & R_{11}^2 & 2R_{32}R_{33} & 2R_{33}R_{31} & 2R_{31}R_{32} \\ R_{21}R_{31} & R_{22}R_{32} & R_{23}R_{33} & R_{22}R_{33}+R_{23}R_{32} & R_{21}R_{33}+R_{23}R_{31} & R_{22}R_{31}+R_{21}R_{32} \\ R_{31}R_{11} & R_{32}R_{12} & R_{33}R_{13} & R_{12}R_{33}+R_{13}R_{32} & R_{13}R_{31}+R_{11}R_{33} & R_{11}R_{32}+R_{12}R_{31} \\ R_{11}R_{21} & R_{12}R_{22} & R_{13}R_{23} & R_{12}R_{23}+R_{13}R_{22} & R_{13}R_{21}+R_{11}R_{23} & R_{11}R_{22}+R_{12}R_{21} \end{bmatrix} \tag{3-5}$$

for 6 x 6 matrix.

When the rotation is applied to the material property of α-quartz, where **c**, **e**, and **s** represent stiffness matrix, electromechanical coupling matrix, and dielectric matrix, matrices become

$$\mathbf{C} = [\mathbf{R}_{6x6}][\mathbf{c}][\mathbf{R}_{6x6}]', \tag{3-6}$$

$$\mathbf{E} = [\mathbf{R}][\mathbf{e}][\mathbf{R}_{6x6}]', \tag{3-7}$$

and

$$\mathbf{S} = [\mathbf{R}][\mathbf{s}][\mathbf{R}]'. \tag{3-8}$$

where the capital **C**, **E**, and **S** are matrices of AT-cut quartz relative to **c**, **e**, and **s** for α-quartz.

3-2. Electrodeless-QCM Biosensor

3-2-1. Wireless vibration

As mentioned above, QCM is sensitive to molecules adsorbed on the surface. A commercially used QCM, applying metallic coating on both side of quartz crystal as electrodes, like Fig. 3-4 (a), would largely damp the resonance because of the elastic difference between quartz to metallic electrodes and would show difficulty in detecting small molecules such as Aβ peptide (~4.3 kDa for monomers). Therefore, the electrodeless configuration is necessary, where the metal electrodes are removed from our QCM as in Fig. 3-4 (b). The signal is transduced by two antennas placed "over" the quartz. This configuration has two advantages. First, it prevents the quartz from the energy loss which is caused by elastic difference. Second, the quartz can still be excited under the electric field generate between the antennas. The detail of the wireless

excitation method can be found in reference 41 and 43.

3-2-2. Amyloid β sensor and sensing system

In order to let the WE-QCM biosensor to recognize our target, $A\beta_{1\text{-}40}$ monomer, we modified the bare surface by immobilizing $A\beta_{1\text{-}42}$ seeds (short fibrils) with non-specific adsorption.

When Aβ monomers are attached to the QCM surface, the effective mass of the resonator system increases. In the Sauerbrey equation, the deposited mass on QCM is treated in such a way that it was an extension of thickness of the underlying quartz [22]. The relation is defined as

$$\Delta f_{mass} = -\frac{v_s n}{2\rho_q A D^2}(\Delta m), \tag{3-7}$$

or

$$= -\frac{2nf_0^2}{A\sqrt{\rho_q \mu_q}}(\Delta m). \tag{3-8}$$

Where Δf is resonance frequency difference to the original frequency without mass loading, Δm is the adsorbed mass on WE-QCM surface, f_0 is the resonance frequency the quartz is without mass loading, n is the overtone factor, ρ_q is the mass density of the quartz crystal, μ_q is the shear stiffness of the quartz crystal, and A is the effective sensing area which is the whole surface of quartz in WE-QCM. Hence the frequency shift is proportion to surface mass change, inversely.

However, a QCM immersed in liquid is not only affected by the adsorbed mass, but also by the viscosity of liquid. Based on the concept, Kanazawa *et al*. derived the resonance frequency change by viscosity [25], where

$$\Delta f_{viscosity} = -\sqrt{\frac{n\rho_s \eta_s f_0^3}{\pi \rho_q \mu_q}} \tag{3-9}$$

with mass density (ρ_s) and the viscosity (η_s) of the solution. Therefore, the frequency

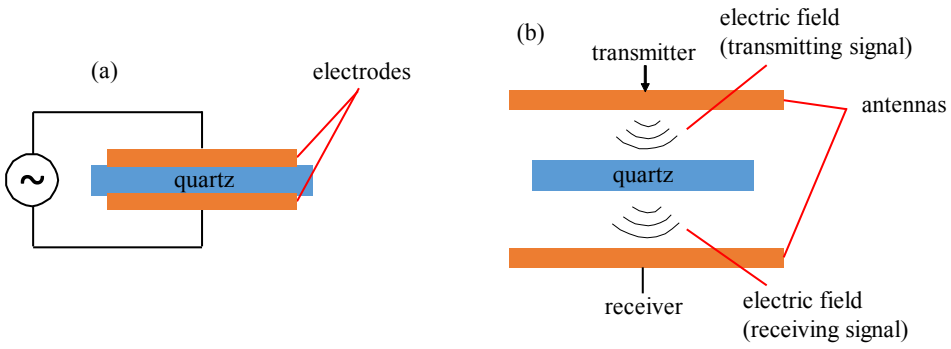

Fig. 3-4 (a) The configuration of commercially used QCM and the (b) wireless excitation of WE-QCM where electrodes are replaced with antennas.

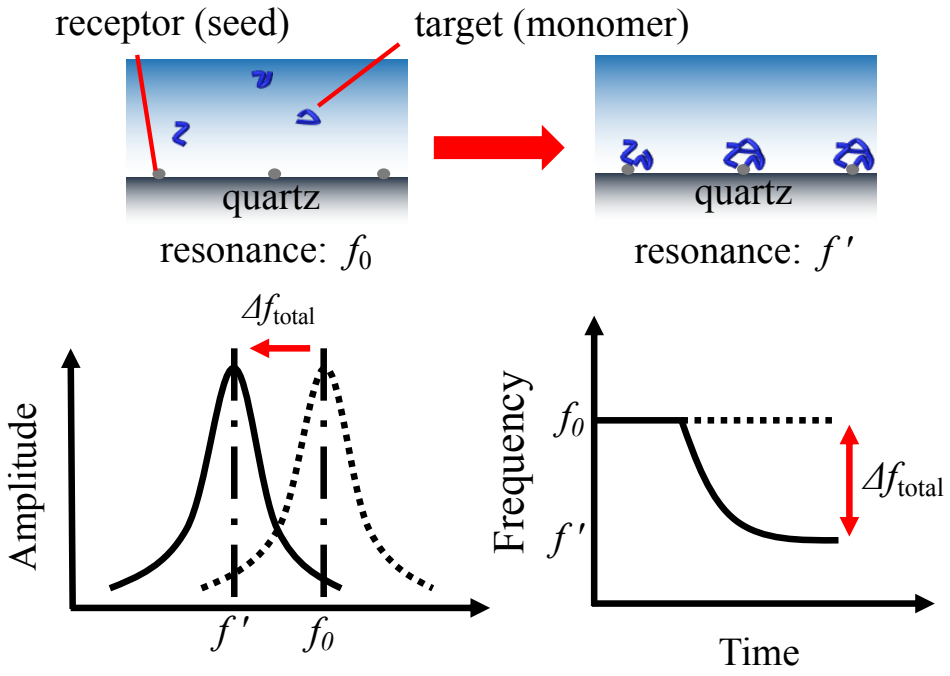

Fig. 3-5 The relation between the resonance frequency to the surface change of WE-QCM where f_0 is the frequency when no monomer was attached, and f' is the frequency dropped from f_0 because of the number of monomers attached to the WE-QCM surface increases, where the surface mass increased with viscosity increased because the shear movement on the surface became harder due to the viscoelastic difference of monomer to quartz.

shift equation becomes

$$\Delta f_{total} = \Delta f_{mass} + \Delta f_{viscosity} = -\left(\frac{2nf_0^2\Delta m}{A\sqrt{\rho_q\mu_q}} + \sqrt{\frac{n\rho_s\eta_s f_0^3}{\pi\rho_q\mu_q}}\right), \quad (3\text{-}10)$$

which is called the modified Sauerbrey equation, and the relationship is shown in Fig. 3-5.

3-3. MEMS QCM Biosensor

3-3-1. The introduction of MEMS packaged WE QCM

The technique of WE-QCM has been developed in 2006 [41], and becomes very promising for many applications in the bio-sensing technology, including ultra-sensitivity in distinguishing concentration differences in molecule solution [55], multichannel in determining the specificity of antibody [83], morphology monitoring by combining WE-QCM with the total-internal-reflection fluorescence microscopy (TIRFM) [60, 84], and availability of very-high and ultra-high frequency sensing [54, 85]. Taking advantage of the WE-QCM with a high frequency quartz, it would have a better sensitivity on the surface as well.

However, many problems emerged for high-frequency application. The quartz is

a very fragile material and becomes easier to fail at high frequency (the quartz has to be very thin for high-frequency application) even transporting the quartz for cleaning yields the possibility of breaking. Another issue is that, WE-QCM uses two silicon rubbers to hold the quartz, causing unfavorable leakage of the vibration energy, resulting in lower quality factor (Q factor: intensity ratio) and then lower intensity. Fortunately, Kato *et al*. came up with an idea of packaging the quartz crystal of WE-QCM [42]. The package consists of three layers in glass-silicon-glass pattern and aligns with a microchannel (Figs. 3-6 (a) and (b)). While the package is strong against piranha solution (acid for quartz cleaning), the transportation via the package reserves the safeties of the quartz.

In our package, the quartz crystal was lightly supported with glass and silicon micro-pillars on both surfaces and hemispheric walls on both side of the four edges as shown in Fig. 3-6 (c). This prevents the quartz from tight clamping or holding, therefore prevents the vibration energy from leaking. This configuration is excellent not only in well preservability of quartz but also in maintaining high Q factor of the WE-QCM.

Since four overtones are involved in our viscoelasticity evaluation, the high Q

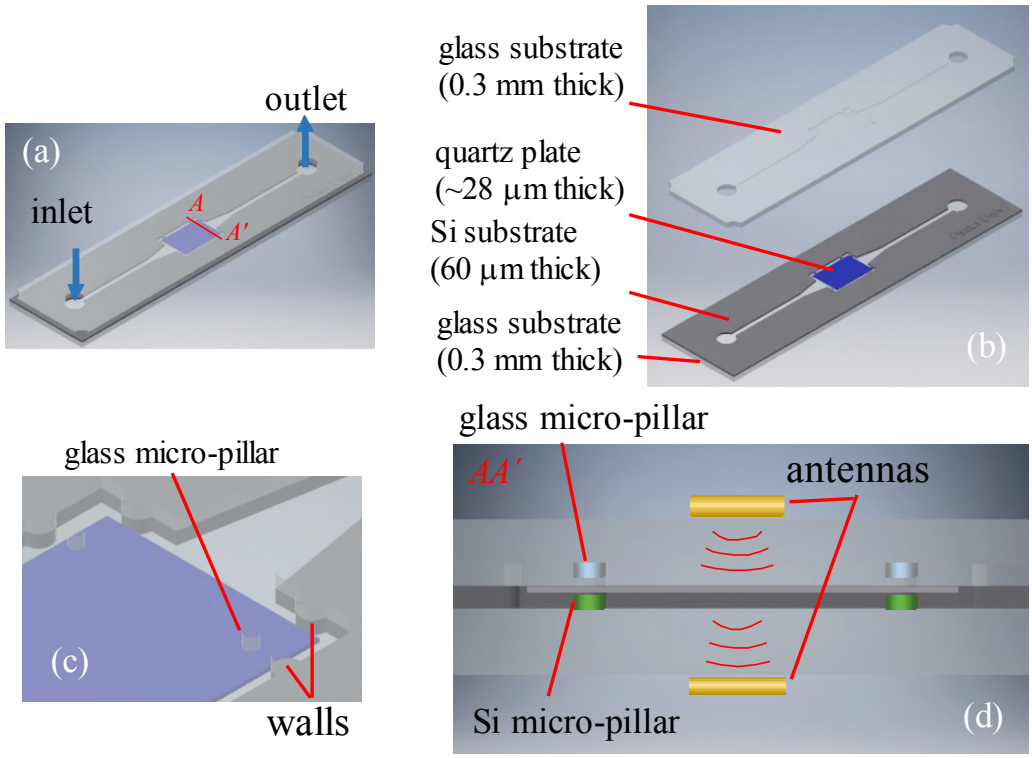

Fig. 3-6 The configuration of the MEMS packaged WE-QCM. Where (a) indicates the assembly drawing with solution flow indicated and (b) shows the exploded drawing of MEMS QCM. (c) provides a close up look at the camber where micro-pillars and walls that hold the quartz lightly and (d) illustrate the wireless excitation from *AA′* cross section view (refer to Fig. 3-6 (a)). The inlet and outlet are interchangeable.

factor of MEMS QCM is promising because it eliminates the energy loss, giving higher overtones a good Q factor [86, 87], and solved the problem of having a relatively weaker stability in overtone [88].

3-3-2. Fabrication of MEMS QCM

The MEMS QCM package consists of three layers: the upper glass cover (300 μm), the silicon in middle (60 μm), and the bottom glass substrate (300 μm). The quartz crystal is embedded in the center of the microchannel, supported by silicon and glass micro-pillars, and four hemispheric walls at the four edges. The wall is silicon-glass layered based on the structure of the package. The microchannel is stretched along the two longer ends, which results a total volume of about 0.94 μl. The dimension of chamber which held the quartz was about 2.7 x 1.9 mm^2 and 150 μm in thickness. The micro-pillars are 0.1 mm and the walls are 0.2 mm in diameter, which narrows the chamber for QCM to about 2.5 x 1.7 mm^2 and 30 μm in thickness, so the quartz can fit in and with merely extra space for moving.

The fabrication is separated into three steps as shown in Fig. 3-7: upper glass cover,

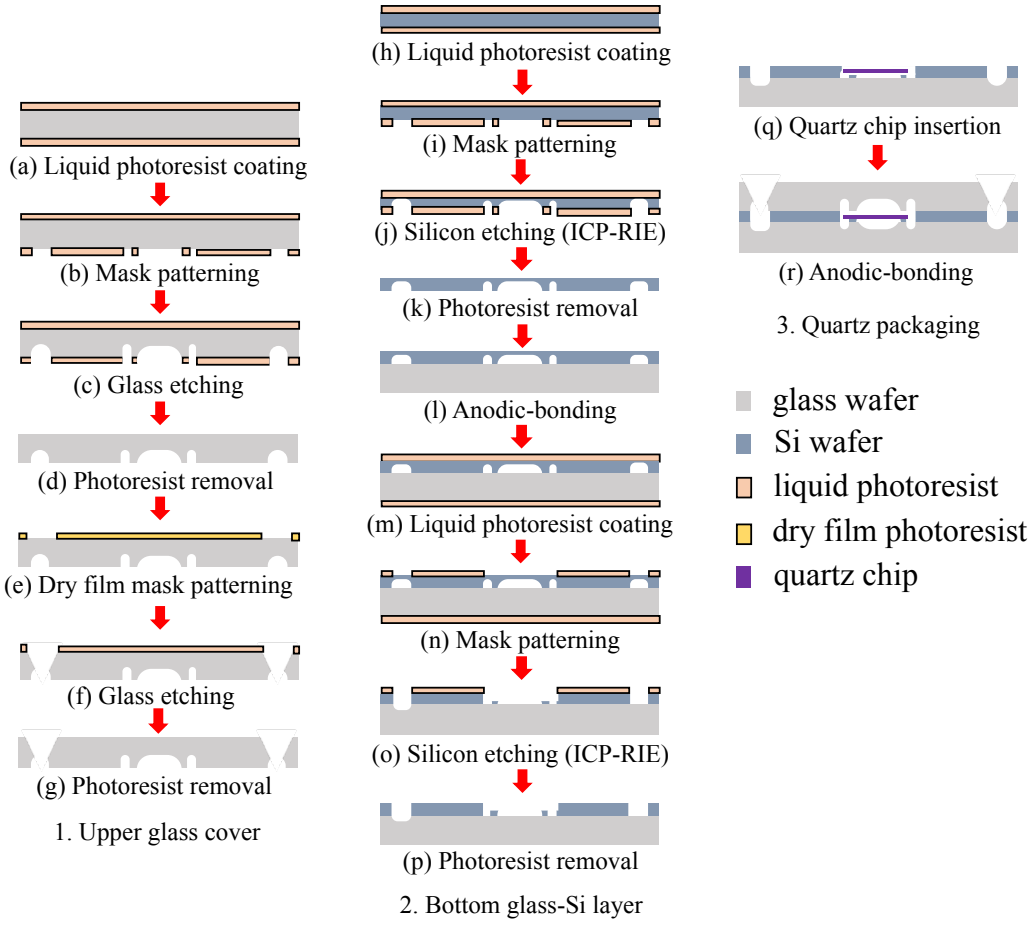

Fig. 3-7 Procedure flow of MEMS QCM fabrication, which is separated into three steps; including upper glass cover, bottom glass-Si layer, and quartz packaging.

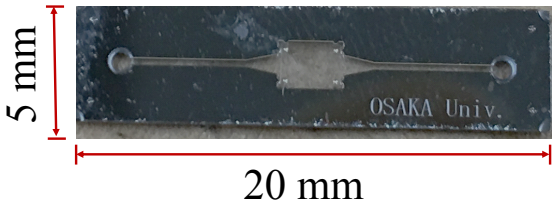

Fig. 3-8 Appearance of MEMS packaged QCM where one can see clearly the glass micro-pillars and hemispheric walls on the edges of the chamber in center.

bottom glass-Si layer, and quartz packaging. For upper glass cover, a 4-inch glass wafer was coated with liquid photoresist mask (a). The micro-pillars and flow channel were patterned on the bottom for etching (b). Then, the wafer was applied with (100) wet etching to form the shape on the bottom surface (c). Afterwards, the wafer was coated with dry film mask (d) and was patterned two-circles with diameter of 1 mm at the two-ends of microchannel on top surface of the wafer (e). It was then etched through the circle as the microchannel exits (f).

For bottom layer, the 4-inch Si wafer was first mask patterned and was dry etched on the bottom with Inductively Coupled Plasma - Reactive Ion Etching (ICP-RIE) to half the thickness (j). Next, the Si layer was performed anodic bonding to another glass substrate (m), and then was etched through the Si layer with ICP-RIE with the same mask pattern (p). The etching solution for glass etching is hydrofluoric acid and for Si etching is $SF_6 + C_4F_8$. (The process is stated in detail in ref. 38 and 39)

In packaging, an AT-cut quartz chip of 1.7 mm x 2.5 mm with a thickness of 28 μm was placed into the chamber of the bottom glass-Si substrate as shown in Fig. 3-7 (r). The quartz crystal was supported by Si micro-pillars on the bottom and Si walls on each side without tight clamping (Fig. 3-6 (c)). Upper glass cover was then placed on top, covering the quartz and the whole substrate, and the package is applied with anodic bonding between the SI in bottom layer and upper glass layer to seal the package (temperature of substrate: 400ºC).

The final product is shown in Fig. 3-8, and the frequency spectra in water for the fundamental mode and 3rd, 5th, and 7th overtones of this MEMS packaged WE-QCM is shown in Fig. 3-9.

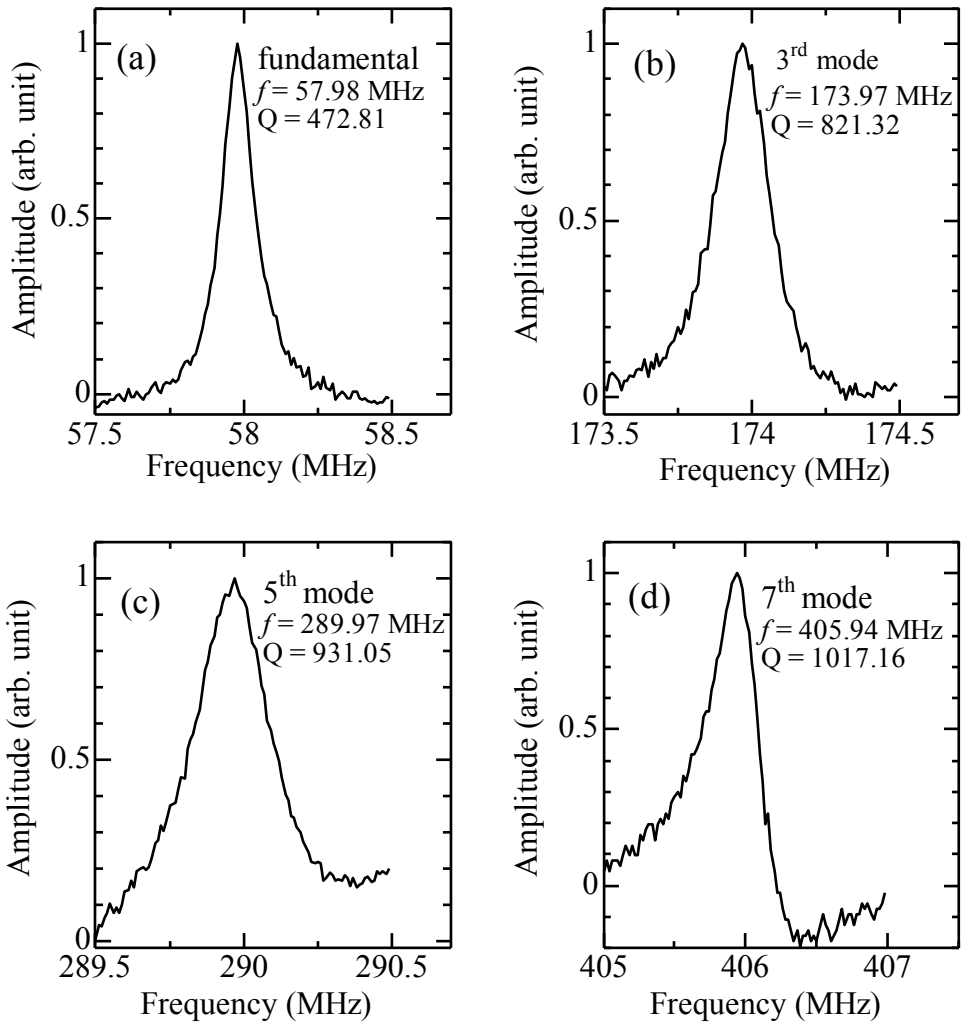

Fig. 3-9 The resonance frequencies of the four overtones of the MEMS packaged QCM ehich will be measured simultaneously in the overtone experiment measured with network analyzer. Where (a) is the fundamental mode (58 MHz), (b) is the 3rd overtone (~174 MHz), (c) is the 5th overtone (~290 MHz), and (d) is the 7th overtone (~406 MHz) with the relative quality factor (Q) derived by the full width at half maximum.

Chapter 4. Viscoelastic Model of Amyloid β QCM Sensor

4-1. Viscoelasticity

Viscoelasticity is a field where both elastic and viscosity characteristics for a material is considered. Inside a material, elasticity is the result of bond stretching along crystallographic planes, where stress and material strain are linear to a factor called stiffness. Viscosity, on the other hand, is the result of inelastic movement of atoms or molecules, where the relationship between stress and material strain depends on time [89], and the difference is as shown in Figs. 4-1 (a) and (b).

It is valuable in knowing the viscoelastic for liquids and biomaterials since the viscoelastic behaviors are more useful in characterizing non-rigid or structural changing materials like Aβ. Viscoelasticity is studied using dynamic mechanical analysis, which applies a complex modulus (dynamic modulus) to describe the relation between stress and material strain. This method is applied to a small oscillatory condition which is achieved from data from either free or forced vibration tests, *e.g.* protein layers on QCM vibration.

Dynamic model describes the phase-lag of stress (σ) and strain (ε), where they are written as

$$\varepsilon = \varepsilon_0 \exp j(\omega t + \phi), \tag{4-1}$$

$$\sigma = \sigma_0 \exp j(\omega t), \tag{4-2}$$

where $j = \sqrt{-1}$, ω is the angular frequency of the oscillation, t is time, and ϕ is the phase-lag between stress and strain. The dynamic modulus expressed the ratio of stress to strain as

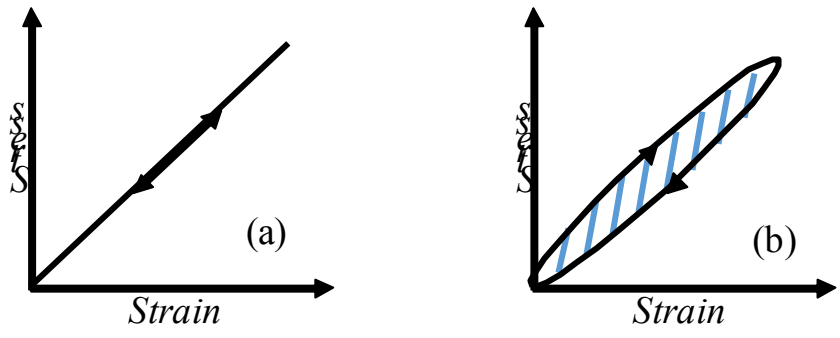

Elastic response Viscoelastic response

Fig. 4-1 The stress-strain relation of (a) elastic material and (b) viscoelastic material. Where the arrows indicate the stress-strain cycle. For viscoelastic material (b) shows the nonlinear cycle with the dashed-area indicating the energy loss.

$$G^* = \frac{\sigma_0}{\varepsilon_0}(\cos\phi - j\sin\phi) = G' + jG'' \quad (4\text{-}3)$$

where. G' is the storage modulus and G'' is the loss modulus in a material.

There are two typical models for analyzing viscoelasticity: Maxwell model and Kelvin-Voigt model. Maxwell model describes the stress relaxation when strain of the material is constant with time, which is appropriate for most polymers [90]. It is simulated as an elastic spring connecting viscos dashpot in series as shown in Fig. 4-2 (a). Kelvin-Voigt model, denote the strain relaxation under a constant stress, and the model can be expressed by the elastic spring and viscos dashpot connecting in parallel as Fig. 4-2 (b) [91, 92].

Among viscoelasticity models, the time relaxation of strain in Kelvin-Voigt model under continuous stress best matches the velocity relaxation from equilibrium point to extreme point in simple harmonic motion (SHM) system such as QCM vibration. Therefore, the description of the model's stress-strain relationship of shear motion (in *x* direction) along the thickness of the system (*y* direction) is

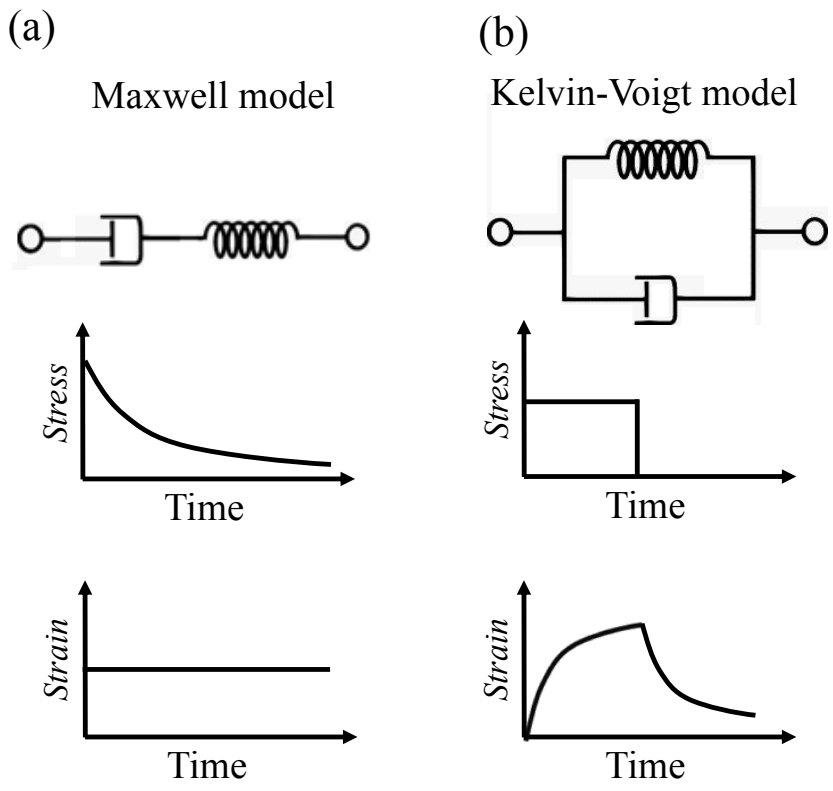

Fig. 4-2 The two viscoelastic models: (a) Maxwell model and its relaxation behavior under constant strain and (b) Kelvin-Voigt model with relaxation behavior.

$$\sigma_{xy} = \sigma_{\mu} + \sigma_{\eta} = \mu \frac{\partial u_x(y,t)}{\partial y} + \eta \frac{\partial v_x(y,t)}{\partial y},$$

$$= \left(\mu + \eta \frac{\partial}{\partial t}\right) \frac{\partial u_x(y,t)}{\partial y}. \quad (4\text{-}4)$$

Where the shear modulus (μ) portion signifies the spring branch and viscosity (η) is the dash-pot branch of Kelvin-Voigt model, and $\partial u_x(y,t)/\partial y$ is the shear strain and $\partial v_x(y,t)/\partial y$ is the time dependent velocity in shear direction. The modulus is chosen to represent the relation in polar form:

$$\mu^* = \mu' + j\mu'' = \mu + j\omega_n \eta. \quad (4\text{-}5)$$

Where μ' is the storage modulus (shear), μ'' is the damping modulus (viscosity), and denotation n is the overtone number of n=1, 3, 5….

4-2. MEMS QCM and Viscoelastic Evaluation

Since the Sauerbrey equation considers that only the mass change on surface would dominate the QCM sensitivity, it becomes inadequate in evaluating viscoelastic materials such as polymer thin film or bio-molecule solution, which are extremely small and the viscos behaviors dominate the material. Therefore, many researches dedicated in developing viscoelastic modeling of QCM.

Viscoelastic models in a QCM assay [93-97] have been built for various surroundings such as gas [94], water [94-96], and amphiphilic overlayer [97, 98]. Most studies have used dissipation (QCM-D) of the resonance vibration for this purpose [91-102], which is, however, affected not only by protein viscoelasticity but also by many experimental conditions such as the solution flow rate, the holding condition of the sensor chip. On the other hand, the overtone frequency change, which is highly stable and much more robust against many experimental conditions, can also be used for evaluating the viscoelasticity.

Since the Aβs in the peptide layer are very soft and unstable in shape, it can be looked as a group of viscoelastic material that can damped the penetration energy. As the penetration depth (δ, as shown in Fig. 4-3) of the quartz resonance (or the effective sensing depth) is inverse proportion to the resonance frequency via dynamic viscosity (N_s) of the liquid ($\delta = \sqrt{2N_s/\omega}$, where $\omega = 2\pi f$). In other words, different depth in the solution coupled with the QCM can be detected by different overtone because of the sensing coverage is different for different overtone responses. It is thus desirable to use only the overtone frequency responses without using dissipation, and a QCM with sufficiently higher frequency is needed for this to improve the sensitivity to viscoelasticity.

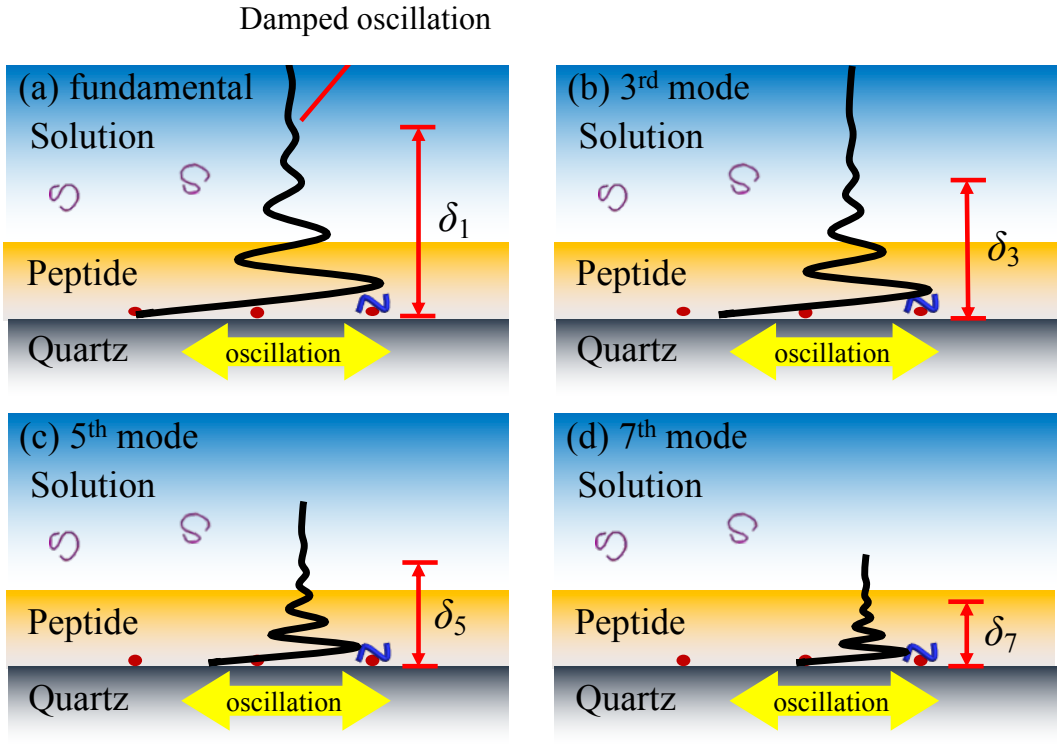

Fig. 4-3 Illustration of the concept of viscoelastic calculation with measuring four overtones simultaneously. (a) shows the dissipation of the QCM shear energy penetrating into peptide and solution for the fundamental mode, (b) is the 3rd mode, (c) is the 5th mode, and (d) is the 7th mode. Where δ is the penetration depth and the depth is different for different resonance frequency.

4-3. 3-layer Model and Inverse Calculation

We assume that a continuous and homogenous layer of Ab peptides growing on WE-QCM between the solution layer and quartz surface. The resonance frequency of such a multilayer system principally depends on five parameters: thickness, viscosity, mass density, and stiffness of the protein layer, and the overtone index n of the resonance frequencies [84, 85, 94]. We then simultaneously measured the frequency change for n=1, 3, 5, and 7 to extract the remaining parameters inversely by the least-squares method.

In the model [84, 85] as illustrated in Fig. 4-4 we have assigned different materials to each layer: First, the WE-QCM is regarded as purely elastic (α-quartz), where the viscosity can be looked as 0. Next, the peptide (Aβ) layer is regarded as a viscoelastic Kelvin-Voigt material [97], where an elastic spring and a dashpot are connected in parallel. Last, the solution layer is considered as a Newtonian fluid, where shear stiffness can be ignored. Here, h, ρ, μ, and η represent thickness, mass density, shear modulus, and viscosity, and ω_n is the angular frequency of the nth overtone. The subscripts s, p, and q represent solution, Aβ peptide, and quartz layer, respectively.

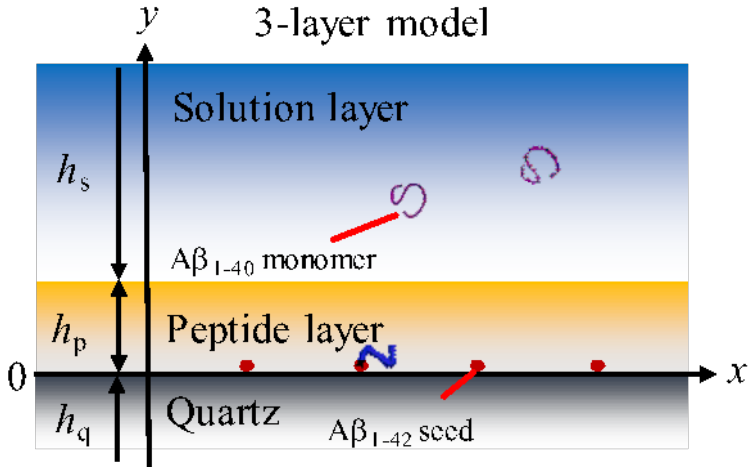

Fig. 4-4 Illustration of the viscoelastic 3-layer model in the calculation with measuring four overtones simultaneously. Where *x*-axis indicates the quartz surface and *y*-axis is the thickness direction of the sensing system. The peptide layer denotes the $A\beta_{1\text{-}42}$ seed and Aβ aggregates and the solution layer is the solution of Aβ monomer.

For the three-layers, the shear-motional equation is expressed as

$$\mu_q \frac{\partial^2 u_x(y_q,t)}{\partial y^2} = -\rho_q \omega^2 u_x(y_q,t) \tag{4-6}$$

for quartz layer,

$$\mu_p^* \frac{\partial^2 u_z(y_p,t)}{\partial y^2} = -\rho_q \omega^2 u_x(y_p,t) \tag{4-7}$$

for peptide layer, and

$$j\omega\eta_s \frac{\partial^2 u_x(y_s,t)}{\partial y^2} = -\rho_q \omega^2 u_x(y_s,t) \tag{4-8}$$

for solution layer. Where ω is the angular frequency of QCM vibration.

The general solution of each layer can be expressed as

$$u_x(y,t) = \left(C_1 e^{-\xi y} + C_2 e^{\xi y}\right) e^{j\omega t}. \tag{4-9}$$

with $\xi = \alpha + jk$. Where α is the attenuation coefficient

$$\alpha = \frac{1}{\delta}\sqrt{\frac{\sqrt{1+\chi^2}-\chi}{1+\chi^2}}, \tag{4-10}$$

and k is the wave number

$$k = \frac{1}{\delta}\sqrt{\frac{\sqrt{1+\chi^2}+\chi}{1+\chi^2}}. \tag{4-11}$$

Where χ is the ratio of storage modulus to damping modulus. δ is the viscous penetration depth:

$$\chi = \frac{\mu}{\eta\omega}, \quad \delta = \sqrt{\frac{2\eta}{\rho\omega}}. \tag{4-12}$$

The general solution of the layers become:

$$u_x(y_q,t) = \left(A_1 e^{-\xi_q y} + A_2 e^{\xi_q y}\right)e^{j\omega t}, \xi_q = jk_q = j\sqrt{\frac{\rho_q \omega^2}{\mu_q}},$$

$$u_x(y_p,t) = \left(B_1 e^{-\xi_p y} + B_2 e^{\xi_p y}\right)e^{j\omega t}, \xi_p = \alpha_p + jk_p = j\sqrt{\frac{\rho_p \omega^2}{\mu_p^*}}, \qquad (4\text{-}13)$$

$$u_x(y_s,t) = \left(C_1 e^{-\xi_s y} + C_2 e^{\xi_s y}\right)e^{j\omega t}, \xi_s = \alpha_s + jk_s = \sqrt{\frac{j\rho_s \omega^2}{\eta_s}},$$

with the stresses of each layer

$$\sigma_{xy}(y_q,t) = \mu_q \frac{\partial u_x(y_q,t)}{\partial y} = \mu_q\left(-A_1\xi_q e^{-\xi_q y} + A_2\xi_q e^{\xi_q y}\right)e^{j\omega t},$$

$$\sigma_{xy}(y_p,t) = \mu_p^* \frac{\partial u_x(y_p,t)}{\partial y} = \mu_p^*\left(-B_1\xi_p e^{-\xi_p y} + B_2\xi_p e^{\xi_p y}\right)e^{j\omega t}, \qquad (4\text{-}14)$$

$$\sigma_{xy}(y_s,t) = \eta_s \frac{\partial v_x(y_s,t)}{\partial y} = j\omega\eta_s\left(-C_1\xi_s e^{-\xi_s y} + C_2\xi_s e^{\xi_s y}\right)e^{j\omega t}.$$

For the velocity in shear direction is

$$v_x(y,t) = \dot{u}_x = j\omega u_x.$$

Next, the boundaries at the up-end of solution layer and the down-end of quartz layer are considered free where the shear stress at the end of the solution is 0, and each interface (solution-peptide and peptide-quartz) are thought continuity of shear stress and displacement.

For the end of solution layer where $y = h_p + h_s$ and shear stress = 0,

$$j\omega\eta_s\left(-C_1\xi_s e^{-\xi_s(h_p+h_s)} + C_2\xi_s e^{\xi_s(h_p+h_s)}\right)e^{j\omega t} = 0,$$

$$C_1 e^{-2\xi_s h_s} = C_2 e^{2\xi_s h_p}. \qquad (4\text{-}15)$$

and for the up-end of peptide layer $y = h_p$ and no-slip condition between solution layer and peptide layer ($v_s = v_p$),

$$j\omega\left(B_1 e^{-\xi_p h_p} + B_2 e^{\xi_p h_p}\right)e^{j\omega t} = j\omega\left(C_1 e^{-\xi_s h_p} + C_2 e^{\xi_s h_p}\right)e^{j\omega t},$$

$$B_1 e^{-\xi_p h_p} + B_2 e^{\xi_p h_p} = e^{-\xi_s h_p}\left(C_1 + C_2 e^{2\xi_s h_p}\right). \qquad (4\text{-}16)$$

putting equation (4-15) into (4-16), then

$$B_1 e^{-\xi_p h_p} + B_2 e^{\xi_p h_p} = C_1 e^{-\xi_s h_p}\left(1 + e^{-2\xi_s h_s}\right),$$

$$C_1 e^{-\xi_s h_p} = \frac{B_1 e^{-\xi_p h_p} + B_2 e^{\xi_p h_p}}{1 + e^{-2\xi_s h_s}}. \qquad (4\text{-}17)$$

and for continuity in shear stress

$$\mu_p^*\left(-B_1\xi_p e^{-\xi_p h_p} + B_2\xi_p e^{\xi_p h_p}\right) = j\omega\eta_s\left(-C_1\xi_s e^{-\xi_s h_p} + C_2\xi_s e^{\xi_s h_p}\right),$$

$$= j\omega\eta_s\xi_s C_1 e^{-\xi_s h_p}\left(-1 + e^{-2\xi_s h_s}\right). \qquad (4\text{-}18)$$

With equation (4-17) and (4-18), we have

$$\frac{\mu_p^*}{j\omega}\left(-B_1\xi_p e^{-\xi_p h_p} + B_2\xi_p e^{\xi_p h_p}\right) = \eta_s\xi_s \frac{B_1 e^{-\xi_p h_p} + B_2 e^{\xi_p h_p}}{1 + e^{-2\xi_s h_s}}\left(-1 + e^{-2\xi_s h_s}\right),$$

$$= -\eta_s\xi_s\left(B_1 e^{\xi_p h_p} + B_2 e^{\xi_p h_p}\right)\tanh(\xi_s h_s). \qquad (4\text{-}19)$$

Letting

$$\kappa_p = \frac{\mu_p^*}{j\omega_n}, \kappa_s = \eta_s,$$

Equation (4-18) becomes

$$\kappa_p\xi_p\left(-B_1e^{-\xi_p h_p} + B_2e^{\xi_p h_p}\right) = -\kappa_s\xi_s\left(B_1e^{-\xi_p h_p} + B_2e^{\xi_p h_p}\right)\tanh(\xi_s h_s),$$

$$B_1 = B_2e^{2\xi_p h_p}\frac{\kappa_p\xi_p+\kappa_s\xi_s\tanh(\xi_s h_s)}{\kappa_p\xi_p-\kappa_s\xi_s\tanh(\xi_s h_s)},$$

$$B_1 = B_2Ae^{2\xi_p h_p}, \tag{4-20}$$

where the solution for peptide layer

$$A = \frac{\kappa_p\xi_p+\eta_s\xi_s\tanh(\xi_s h_s)}{\kappa_p\xi_p-\eta_s\xi_s\tanh(\xi_s h_s)}. \tag{4-21}$$

The velocity of the peptide layer is

$$v_x(y_p,t) = j\omega B_2\left(Ae^{2\xi_p h_p}e^{\xi_p y} + e^{\xi_p y}\right)e^{j\omega t}. \tag{4-22}$$

For y=0 where is the quartz-peptide interface, the shear velocity is

$$v_0 = j\omega B_2\left(Ae^{2\xi_p h_p} + 1\right)e^{j\omega t}. \tag{4-23}$$

Therefore, for the peptide layer

$$v_x(y_p,t) = v_0\frac{\left(e^{2\xi_p y}+Ae^{2\xi_p h_p}\right)}{e^{\xi_p y}\left(Ae^{2\xi_p h_p}+1\right)}, \tag{4-24}$$

$$u_x(y_p,t) = u_0\frac{\left(e^{2\xi_p y}+Ae^{2\xi_p h_p}\right)}{e^{\xi_p y}\left(Ae^{2\xi_p h_p}+1\right)}, \tag{4-25}$$

$$\sigma_{xy}(y_p,t) = \sigma_0\frac{\left(e^{2\xi_p y}-Ae^{2\xi_p h_p}\right)}{e^{\xi_p y}\left(-Ae^{2\xi_p h_p}+1\right)}. \tag{4-26}$$

For y equals the peptide-solution interface h_p, the solution layer

$$u_x(y_s,t) = u_{hp}\frac{\left(e^{2\xi_s(h_p+h_s)}e^{-\xi_s y}+e^{\xi_s y}\right)}{e^{\xi_s h_p}\left(e^{2\xi_s h_s}+1\right)}, \tag{4-27}$$

$$\sigma_{xy}(y_s,t) = \sigma_{hp}\frac{\left(-e^{2\xi_s(h_p+h_s)}e^{-\xi_s y}+e^{\xi_s y}\right)}{e^{\xi_s h_p}\left(-e^{2\xi_s h_s}+1\right)}. \tag{4-28}$$

By applying the well-known equation from QCM-D modeling [95-99], the frequency equation and the dissipation equation are

$$\Delta f_n \cong \frac{1}{2\pi\rho_q h_q}Im\left(\kappa_p\xi_p\frac{1-Ae^{2\xi_p h_p}}{1+Ae^{2\xi_p h_p}}\right), \tag{4-29}$$

and

$$\Delta D_n \cong \frac{-1}{\pi\rho_q h_q}Re\left(\kappa_p\xi_p\frac{1-Ae^{2\xi_p h_p}}{1+Ae^{2\xi_p h_p}}\right). \tag{4-30}$$

For A in (4-21) is the solution of peptide layer, and

$$A = \frac{\kappa_p\xi_p+\eta_s\xi_s\tanh(\xi_s h_s)}{\kappa_p\xi_p-\eta_s\xi_s\tanh(\xi_s h_s)},\ \kappa_p = \frac{\mu_p^*}{j\omega_n},$$

Table III The constants used in the viscoelastic calculation.

Solution layer	Peptide layer	Quartz layer [103]
ρ_s 1 g/cm^3	ρ_p 1.1 g/cm^3	ρ_q 2.648 g/cm^3
h_s 1 mm		h_q 28 μm
η_s 1 μPa*s		μ_q 30 Gpa

$$\xi_p = \sqrt{-\frac{\rho_p \omega_n^2}{\mu_p^*}},\ \xi_s = \sqrt{\frac{j\rho_p \omega_n}{\eta_s}}.$$

Because only the resonance frequency is used in this viscoelastic evaluating system, only equation (4-29) is applicable. Furthermore, both sides of WE-QCM are used in sensing, the equation (4-29) should be twice. Where

$$\Delta f_n \cong \frac{1}{\pi \rho_q h_q} Im\left(\kappa_p \xi_p \frac{1-Ae^{2\xi_p h_p}}{1+Ae^{2\xi_p h_p}}\right). \quad (4\text{-}31)$$

We assumed ρ_p to be 1100 kg/m^3 to reduce the ambiguity of calculation because the effect of ρ_p was very small comparing to other parameters [84]. The parameters of quartz are referring to the work by Ogi *et al*. [101] and the parameter of the solution are assigned as water listed in Table III. The three parameters (h_p, μ_p, and η_p) are then inversely determined from four overtone frequencies measured simultaneously.

Chapter 5. Frequency Response and Surface Analysis of Amyloid β Aggregation

5-1. Solution Preparation

5-1-1. $A\beta_{1-42}$ seed solution

$A\beta_{1-42}$ monomer (4349-v, Peptide Institute, Ibaraki, OSAKA, Japan) was dissolved in dimethyl sulfoxide (DMSO) with magnetic stirring for 10 min at 150 rpm. It was then diluted in acetate buffer solution (ABS, pH = 4.6) to a concentration of 50 μM, where the volume ratio of DMSO to ABS was 1 to 5. This seed solution was then stirred for 24 h at 1200 rpm to form the fibrils [54, 104]. The solution was then exposed to 200-W ultrasonic irradiation under 26 kHz to condense the small fibrils to obtain the seeds. The solution was diluted by ABS to obtain the seed solution with concentration of 16 μM total monomer. The formation of fibril seed was confirmed by Thioflavin-T (ThT) fluorescence experiment [104]; the ThT level of the seed solution was higher than that of the monomer solution by a factor of ~100, confirming that β-sheet structure was developed.

5-1-2. $A\beta_{1-40}$ monomer solution

$A\beta_{1-40}$ monomer (4307-v, Peptide Institute, Ibaraki, OSAKA, Japan) was dissolved in DMSO and was diluted in ultrapure water until a final concentration of 10 μM total monomer. The ratio of DMSO to ultrapure water was 1:20. Note that the flowing solution should be prepared right before its injection into the QCM measurement.

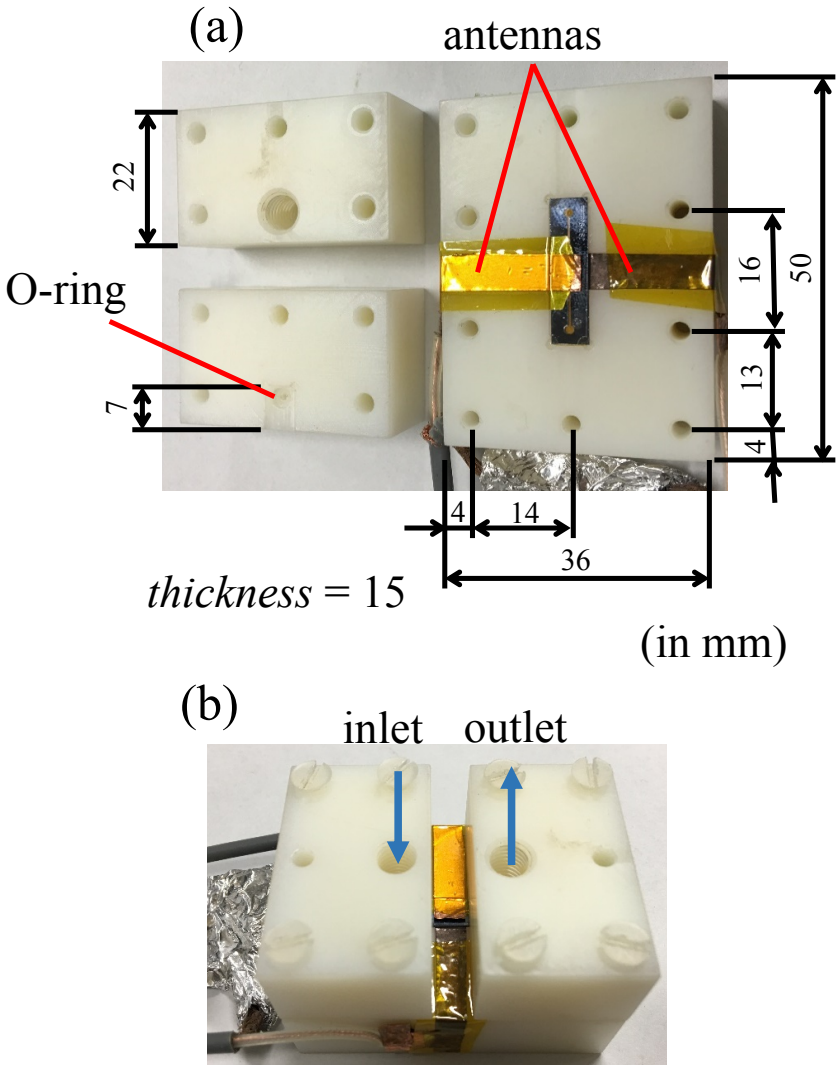

Fig. 5-1 (a) is the part-view of MEMS QCM sensor cell with MEMS QCM fitted into the notch with copper tapes (antennas) on both side of the package. (b) is the assembled MEMS QCM sensor cell with solution flow indicated. Inlet and outlet are interchangeable.

5-2. Overtone Experiments

5-2-1. Preparation of MEMS QCM biosensor

In order to let our QCM biosensor recognize $A\beta_{1\text{-}40}$, the QCM surface should be immobilized with $A\beta_{1\text{-}42}$ seeds. First, we injected the piranha solution (7:3 of 98% H_2SO_4 to 33% H_2O_2) into the package to cover the quartz and left for 10 min to wash the chip. Then the chips were rinsed with ultrapure water (until pH 7), and cleaned with

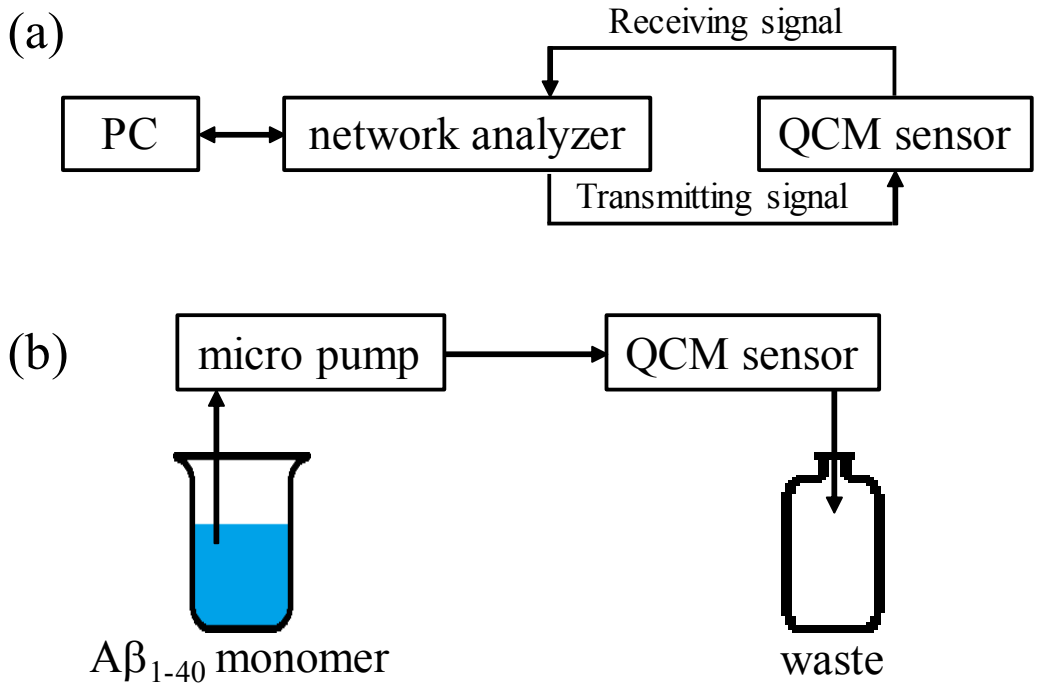

Fig. 5-2 (a) The signal flow and (b) the liquid flow of the QCM sensing system.

UV-ozone for 15 min. It was then immersed with the $A\beta_{1-42}$ seed solution and incubated for ~20 h under $4^{o}C$ to immobilize the seeds onto the quartz crystal by nonspecific adsorption. The chip was washed with ultrapure water and then set into the sensor cell as shown in Fig. 5-1.

The signal flow and the liquid flow can refer to Fig 5-2. Two copper tapes, served as flat antennas in this experiment, were pasted on two sides of the MEMS QCM and is installed into the sensing cell as shown in Fig. 5-1 (a). The antennas were connected to a network analyzer (ZNB, ROHDE&SCHWARZ) via BNC cables, and the transmission signal (S12) was monitored by the network analyzer and the resonance frequency was calculated and memorized by a programmed PC as the signal flow shown in Fig. 5-2 (a). A micro-piezoelectric pump was used to induce solution flow where the flow connection is shown in Fig. 5-2 (b). The experiment setup is shown in Fig. 5-3.

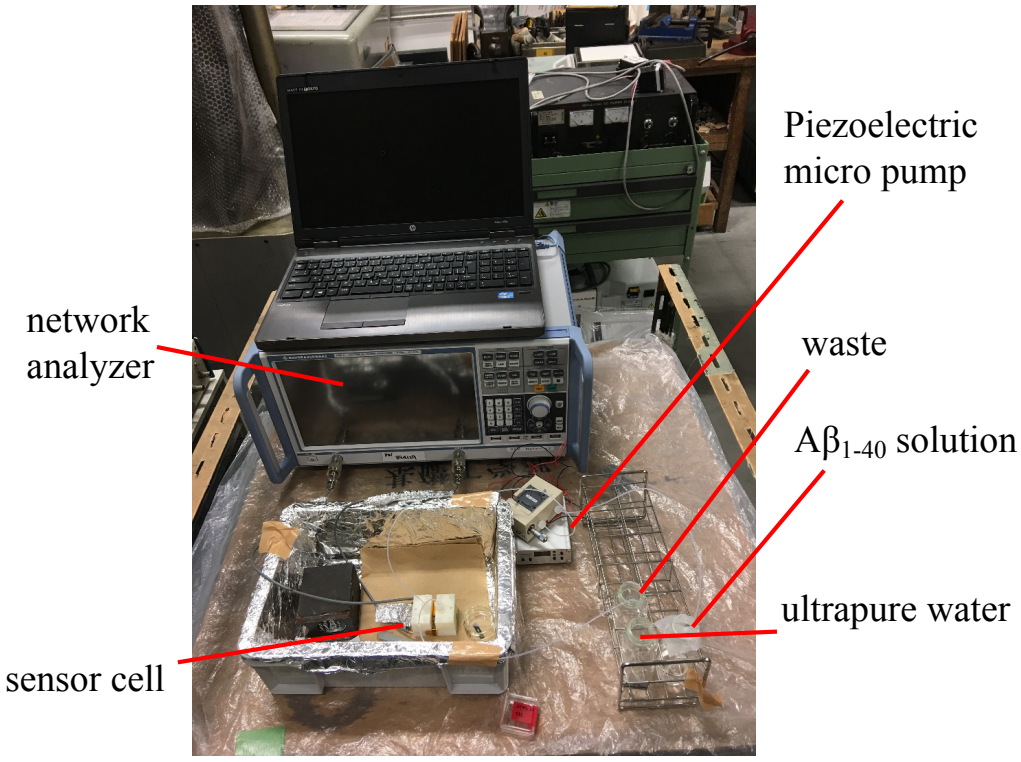

Fig. 5-3 MEMS QCM sensing system setup for overtone experiment.

5-2-2. Experiment procedure

Initially, ultrapure water was flowed into the sensor cell over the quartz surfaces as the carrier solution. When the four frequencies became stable, the $A\beta_{1\text{-}40}$ flowing solution was injected with the flow rate 20 μl/min. (The solution would fill the microchannel in 2.4 s.) We monitored the resonance frequencies of the fundamental (58 MHz), 3rd (174 MHz), 5th (290 MHz), and 7th (406 MHz) modes simultaneously. The experiment is performed under room temperature.

The flow chart of the program for sensing is patterned as shown in Fig. 5-4. A programmed PC was connected to the network analyzer with an Ethernet cable. When the program starts, the PC automatically pair up with the network analyzer. Next, we set the frequency spectrum to include the peak of each four overtones to individual channels and the program will calculate and memorize the resonance frequencies from the spectra. The resonance frequency is then compared to the first resonance point measured in the course and is calculated and plotted as frequency shift. The frequencies of all channels are written into a ".dat" data file throughout the course of the measurement. After the experiment, the program is stopped manually, and the data files are retrieved from the PC.

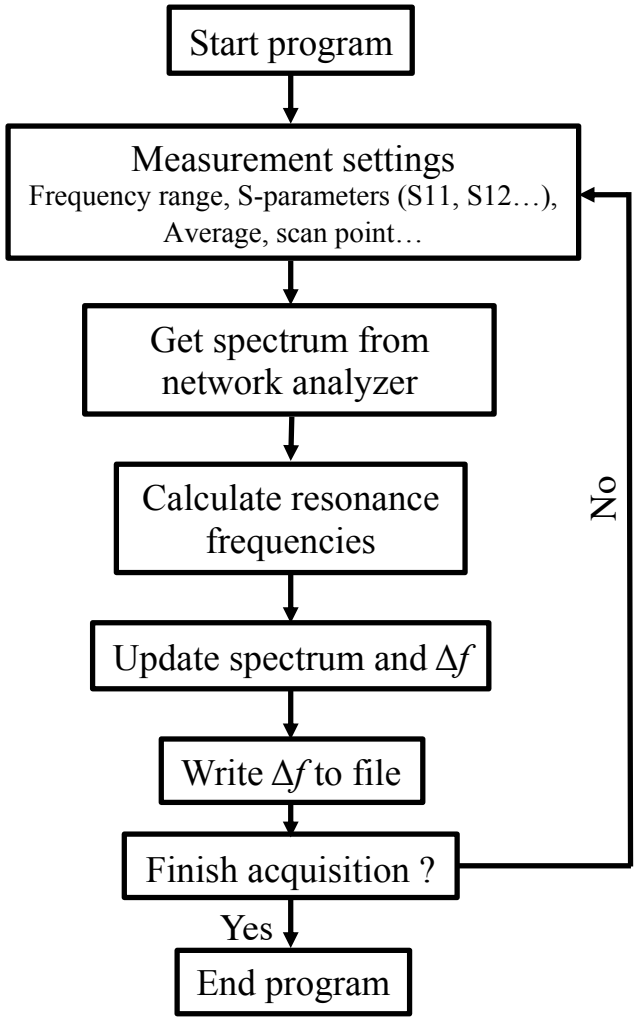

Fig. 5-4 Flow chart of the QCM sensing program.

5-2-3. Result

A typical result for the overtone measurement of $A\beta_{1-40}$ binding to $A\beta_{1-42}$ seeds on the MEMS QCM is shown in Fig. 5-5 (a). (Other independent experimental results are shown in Chapter 6) As shown in Fig. 5-5 (b), the $A\beta_{1-40}$ flow solution arrives at the sensor chip at time 0, and all overtone frequencies drastically drop by 250-300 ppm within 1 h. Then, the frequencies gradually increase until 18 h with slopes of 2.1, 2.8, 2.5, and 1.7 ppm/h for fundamental, 3rd, 5th, and 7th modes, respectively between 10 and 15 h. However, the resonance frequencies significantly increased between 18 and ~22 h (we call this a frequency ramp as shown in Fig. 5-5 (c)), and their slopes also increased to 8.0, 6.6, 6.1, and 10 ppm/h, respectively. Afterward, the frequencies became stable again with slopes of 3.0, 3.5, 3.1, and 3.6, respectively.

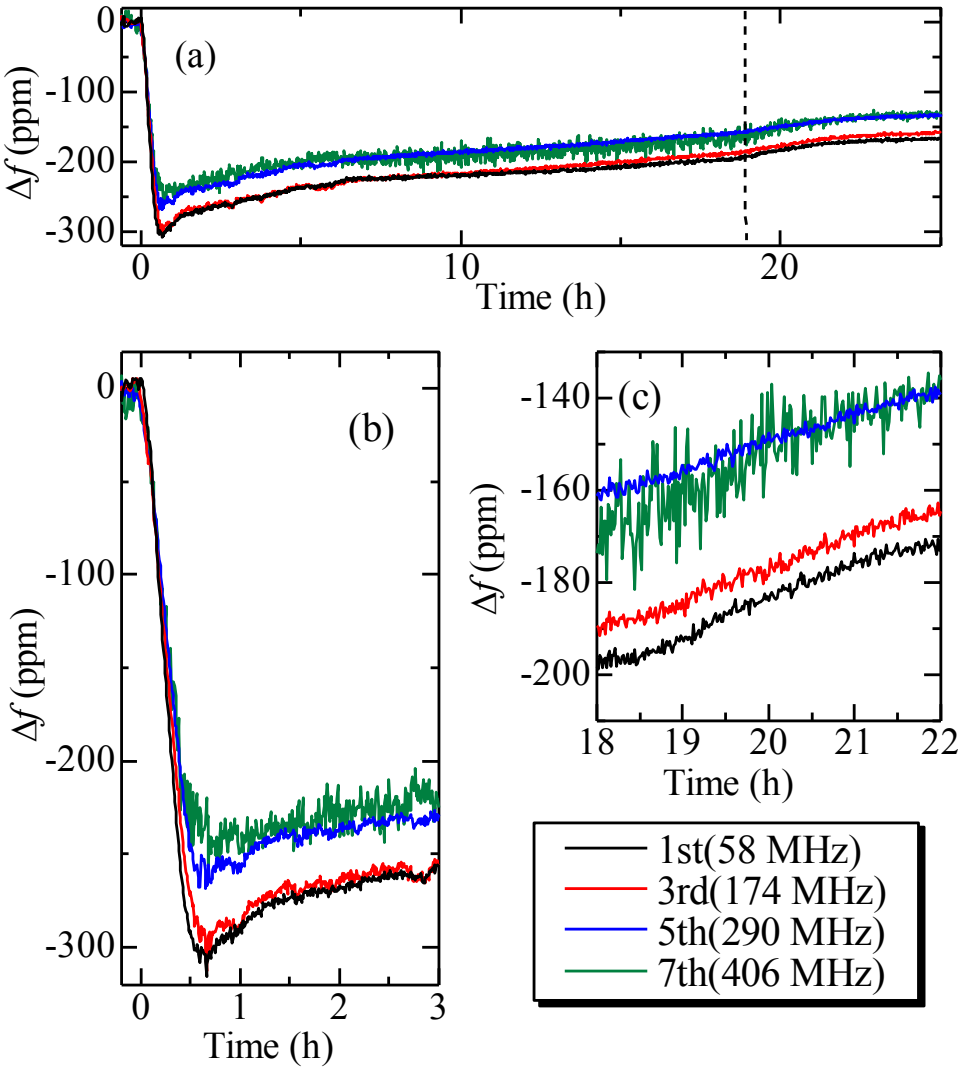

Fig. 5-5 Overtone experiment with fundamental, 3rd, 5th, and 7th modes under Aβ aggregation of $A\beta_{1-40}$ monomer solution flow over the $A\beta_{1-42}$ seeds immobilized on the MEMS QCM. (a) Entire experimental results, with the dash-line indicating the frequency ramp. (b) A close-up figure of (a) during the initial binding of first 3 h. (c) The frequency ramp during 18 h to ~22 h.

5-3. Correlation Experiment

5-3-1. Preparation of WE-QCM biosensor without package

The surface modification for WE-QCM without package was same as the packaged MEMS QCM. The purpose of conducting the aggregation experiment again with the packaged-free candidate is to study the surface morphology of the Aβ aggregate using AFM. The bare quartz chip of 1.7 mm x 2.5 mm area and 28 μm thickness was washed with piranha solution for 10 min, rinsed with ultrapure water, and

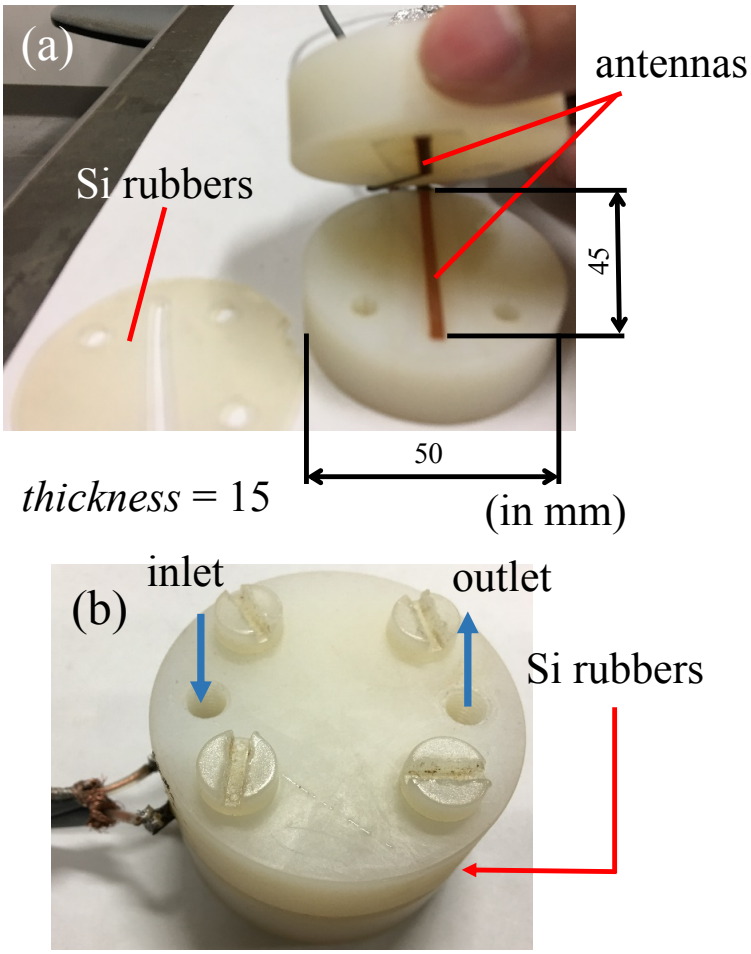

Fig. 5-6 (a) The sensor cell of WE-QCM without package. (b) Assembly of WE-QCM sensor cell where the naked quartz is sandwiched by Si rubbers screwed between the sensor cell with indicating the solution flow. Inlet and outlet are interchangeable.

cleaned with UV-ozone for 15 min. Next, the chip was immersed in the $A\beta_{1\text{-}42}$ seed solution for 20 h at 4^0C. The chip was then sandwiched by silicon rubber sheets and set into the handmade sensor cell as shown in Fig. 5-6 (a) with a flowing-channel volume of 0.3 ml, and two antennas were embedded on both sides of the sensor cell. The Si-rubber sheets were then installed in to the sensor cell as shown in Fig. 5-6 (b). Details are given in refs. 52, 53.

5-3-2. Experiment procedure

This experiment was conducted to understand the dependencies of QCM resonance frequencies and surface morphology on quartz chip. The experiment is based on the result obtained from overtone experiment, and it is performed under similar setup as overtone experiment (Fig. 5-3) and with the package-free WE-QCM sensor cell.

Here, only the fundamental mode was measured in this experiment since we only want to correlate the frequency shift to the overtone experiment. The overtone

experimental result shown in Fig. 5-5 is categorized into three stages in chronical order:

1. At the end of the initial stage (<~ 1h) where the decrease in frequencies reached the utmost, and the slope started to raise to positive.
2. About the 18 h, where the frequencies suddenly increase.
3. About 22 h, when the four frequencies stop increasing (or increase less in contrast to the frequency ramp from 18 h).

The correlation experiment was based on the stage-evolution shown above. Many independent measurements were conducted and was stopped at different stages. For example, one measurement is stopped at the end of stage 1, while another measurement was stopped at stage 2. The flows of signal, liquid, and program are the same as in overtone experiment (Fig. 5-2 and Fig. 5-4). Right after stopping the measurement, the chip is scanned under AFM (Fig. 5-7) to check the surface amorphous of the quartz at relative sudden. The experiment was also held under room temperature,

5-3-3. Atomic force microscope observation

The aggregation reaction that occurred on the surface of the WE-QCM without package was stopped at representative stages: before injection, initial binding (binding stage), before frequency ramp (lag stage), and after frequency ramp (fibril growing stage), and AFM images on the quartz-chip were taken. The AFM used in this work is shown in Fig. 5-7 (a), a tapping-mode using a silicon cantilever with a bending stiffness of 40 N/m was used for the measurements (Figs. 5-7 (b) and (c)). The resonance frequency of the cantilever was near 300 kHz. The scan frequency rate was 1 Hz. The AFM system was produced by Shimadzu Co. Ltd. (SPM A9600) (Fig. 5-7 (a)).

5-3-4. Result

Figs. 5-8 (a)-(c) show a series of independent QCM experimental results, and Figs. 5-8 (e)-(g) show their corresponding AFM images (Other scanned AFM images are shown in Fig. 5-9 and refer to Chapter 6 for more experiments). Before the injection (0 h), we see many dots with ~20 nm in diameter in Fig. 5-8 (d), indicating immobilized $A\beta_{1\text{-}42}$ seeds on the WE-QCM surface. For ~0.65 h after the injection in the first experiment, the frequency dropped tremendously as shown in Fig. 5-8 (a), the corresponding AFM image, in Fig. 5-8 (e), shows larger aggregates than those seen at 0 h. The measurement in Fig. 5-8 (b) shows the gradual increase of the frequency after

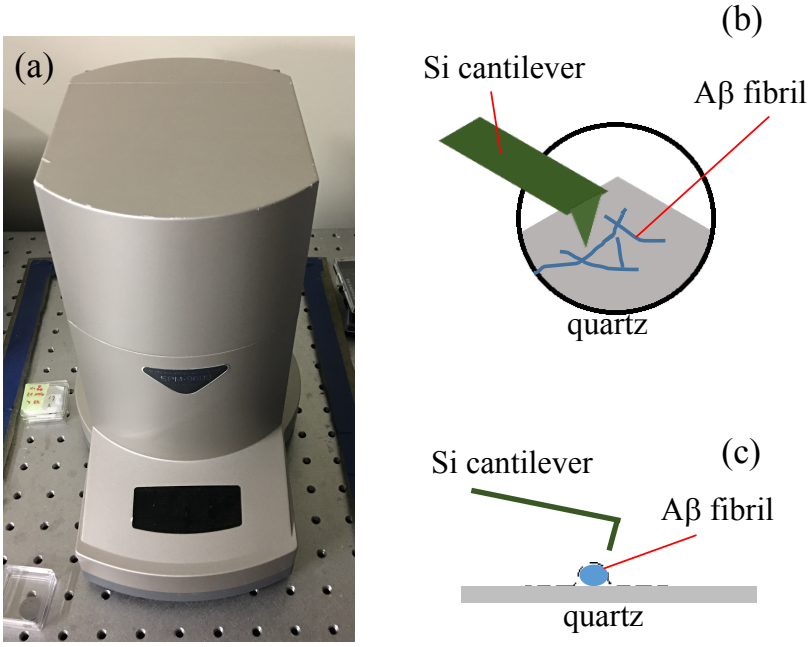

Fig. 5-7 (a) The atomic force microscope from Shimadzu Co. Ltd. (SPM A9600), and the illustrated mechanism of the microscopy (b) in 3D view where Si cantilever would scan through the quartz plate within the chosen region and transmit the responded signal back to the PC for drawing the image and (c) in cross-section view where dash-line denotes the scanning route of the Si cantilever.

the initial binding. The AFM image at 15 h (before the ramp) shows many amorphous-like structures, where the particles grew bigger than the AFM in 0.65 h (as shown in Fig. 5-8 (f), which confirms the similar surface structure to Fig. 5-8 (e)). In Fig. 5-8 (c), the ramp appears at 24.5 h where the slope increased from 0.5 to 15 ppm/h (see the enlarged figure). The Chapter 6 figures (Figs. 6-6 (b) and (c)) also confirm the observation of the ramp in other independent experiments at about 20 h. The AFM images after the ramp clearly show many fine fibrils in the entire region of the quartz surfaces which can be seen in Fig. 5-8 (g) and Fig. 5-9. Therefore, the frequency ramp near 20 h indicates the transition from oligomers to amyloid fibrils.

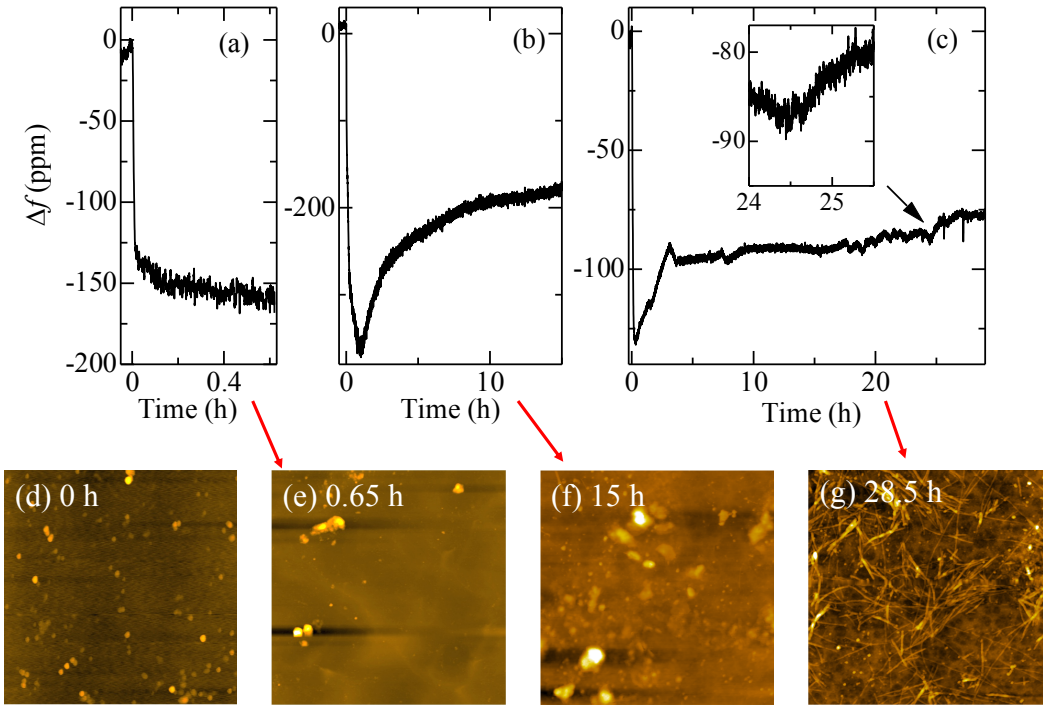

Fig. 5-8 Result of correlation experiment with WE-QCM with only the resonance frequency of fundamental mode (58 MHz) which was stopped at (a) 0.65 h, (b) 15 h, (c) 28.5 h. Note that these are completely independent measurements. (d) shows an AFM image on WE-QCM surface before the injection of monomer solution, and (e)-(g) are AFM images taken right after the correspond experiments (a)-(c). All AFM images are in same scale of 5 μm x 5 μm.

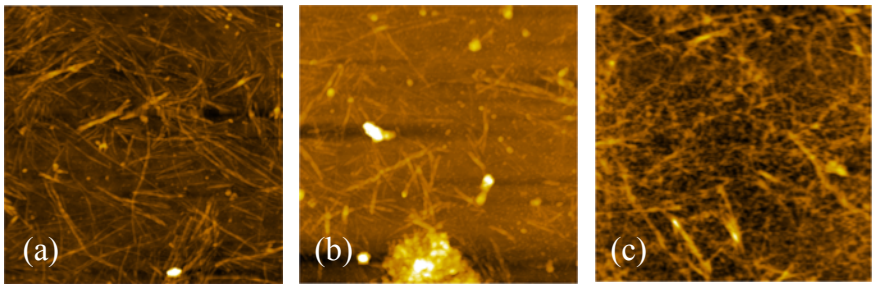

Fig. 5-9 The AFM images of different region on the quartz surface of WE-QCM in experiment Fig. 5-8 (c). Aβ fibrils are observed nearly on the whole area of the WE-QCM surface. All AFM images are in same scale of 5 μm x 5 μm.

Chapter 6. Viscoelastic Analysis and Discussion

6-1. Correlation of Viscoelastic Responses to Surface Transition

In considering the time-dependent evolution of the viscoelastic parameters and surface structure, we separate the results into three stages referring to time evolution in the case of Fig. 5-5 (a). The aggregation proceed on the QCM surface can be seen as Fig. 6-1. First is the binding stage. It is the period starting from the injection of monomer solution until the maximum frequency decrement is reached. Second is the lag stage, which is the long and relatively stable interval from 0.65 h (after the binding stage) to ~18 h (before the frequency ramp). Last is the transition stage from about 18 to 20 h.

Before the arrival of the $A\beta_{1\text{-}40}$ flowing solution, we see dots with diameters of about ~20 nm in the AFM image on the quartz surface (Fig. 5-8 (d)), which we recognize as $A\beta_{1\text{-}42}$ seeds immobilized on the quartz chip. In the binding stage, the significant drops in the frequencies (Fig. 5-5 (b)) cause a large increase in the thickness, viscosity, and shear modulus in the peptide layer (Fig. 6-2 (b)), indicating that the flowing $A\beta_{1\text{-}40}$ monomers are captured by the $A\beta_{1\text{-}42}$ seeds, making the layer thicker and stiffer.

In the early stage of the lag stage (from 1 to 6 h in Fig. 6-2 (a)), the frequencies increase and the thickness decreases, and one may attribute these changes to the detachment of weakly captured monomers from the surface. However, this would not be a principal cause because the viscosity and shear modulus remain unchanged in this period (Figs. 6-2 (a) and (b)); our QCM sensing region is about 20 nm from surface [84], and the averaged shear modulus and viscosity in this region are deduced from the inverse calculation. Because the parameters (thickness, viscosity, and stiffness) depend on the body layer of the system, they should be taken in to account together. As we observed from the binding stage response (<~0.65 h), it is expected that the three

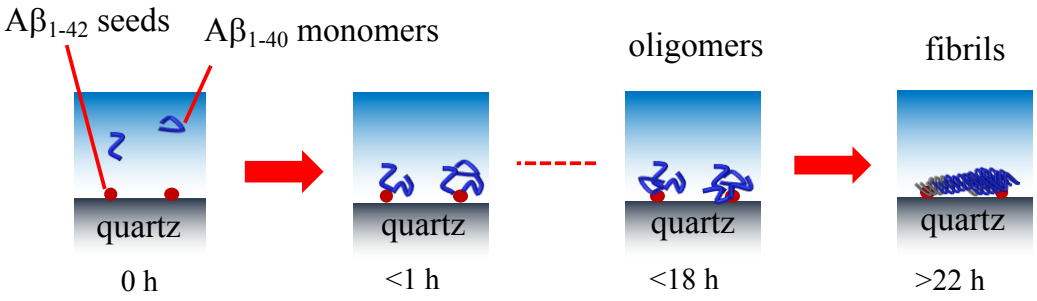

Fig. 6-1 Illustration of the possible condition of Aβ aggregation on the quartz surface.

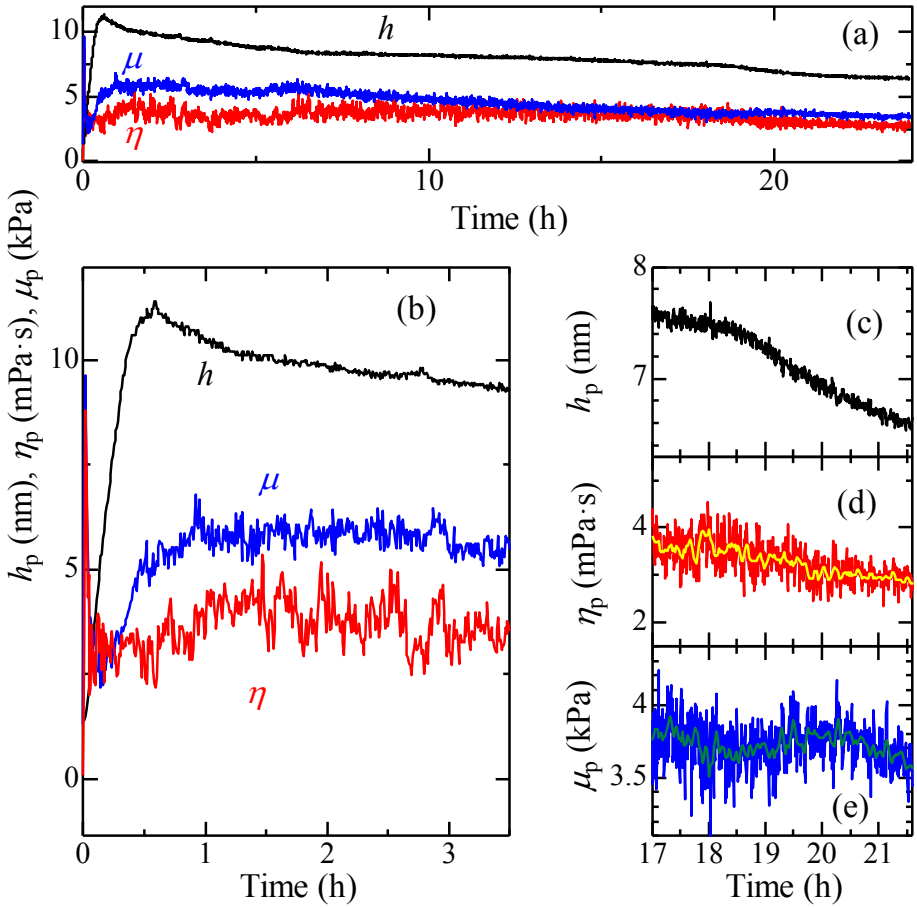

Fig. 6-2 (a) Evolutions of layer thickness, viscosity, and shear modulus of Aβ peptide layer derived from the results in Fig. 5-5. (b) Their changes in the early stage (to 3 h). (c), (d), and (e) show changes in thickness, viscosity, and shear modulus at the frequency ramp.

parameters increased simultaneously when monomers are attached to the seeds immobilized on sensor surface. Detachment of monomers should make all three parameters drop, but this prediction contradicts to the stable viscoelastic properties (shear modulus and viscosity). Therefore, the unchanged average shear modulus and viscosity with decrease in the thickness of the peptide layer indicates increase in the stiffness and viscosity of the aggregates in general. It is also shown in reference 55 that the Aβ particle size increases gradually on the surface, which also contradicts to detachment of weakly captured monomers from the surface. Thus, we consider that the condensation of Aβ aggregates occurs in this period.

After this period in the lag stage (Fig. 5-5 (a)), both thickness and shear modulus decrease gradually, while the viscosity remains unchanged until just before the frequency ramp (Fig. 6-2 (a)). We consider that capturing of Aβ monomers and aggregate condensation [55] continue during this period because of unchanged viscosity,

which again argues against the contribution of detachment of the monomers. The shear-modulus decrease with the stable viscosity suggests that the peptide layer stiffness is nearly unchanged during this period, which is the reason the averaged shear-modulus gradually decreased. The view at this point is confirmed by AFM images (Fig. 5-8 (f)) which show that the aggregates grow on the quartz surface; the deposited Aβ monomers continue to form dense aggregates in the peptide layer, but their structure is not yet fibril.

At the transition stage (18 to 20 h in Fig. 5-5 (a)), a larger increase, compared to the lag stage, has occurred in frequency slopes, which results in the stiffness increase and the thickness decrease (Fig. 6-2 (c)-(e)). This indicates the transition from oligomer to fibril because amyloid fibrils show stiffness much higher than standard protein aggregates [105]. It is verified by AFM images shown in Fig. 5-5 (g) and Fig. 5-9, where dense aggregate structures are replaced by fibril-like structures. Because we failed to find any fibrils just before the frequency ramp, we think that fibrillation occurs simultaneously over nearly the whole area of the quartz crystal. (As shown in Fig. 5-9, the dense fibril structure was observed in different areas of the quartz chip after the frequency ramp.) The significant decrease of the peptide layer thickness in this stage can be caused by the ordering of the aggregates to form the dense fibril. The average shear modulus simultaneously increases, reflecting the much higher stiffness of the formed fibrils. Furthermore, the stiffness increase is also enhanced by the formation of the cross-networking fibril structure overlaying each other as shown in the AFM images (Fig. 5-8 (g) and Fig. 5-9), since the structure is more anti-seismic than single fibrils lying on QCM surface.

6-2. Reproducibility of Viscoelastic Response During Fibril Transition

Throughout the Aβ aggregation, the evaluation of structural transition is the essential. Therefore, a few of overtone experiments and correlation experiments were done in order to closely analyze the reproducibility of the results. Fig. 6-3 shows the independent overtone experiment results. Although the lag stage shows not so identical, the inclined frequency ramp (about 18 h for Fig. 5-5 (a),18 h for Fig. 6-3 (a), 20 h for (b), and 16 h for (c)), which are considered the transition stage of Aβ, can still be determined. The viscoelastic response via the inverse calculation for each individual experiment at the possible transition stage are plotted in Fig. 6-4. All thicknesses of peptide layer agree with the sudden decrease in the response in Fig. 6-2 (c) of the frequency ramp (Figs. 6-4 (a), (d), and (g)). The shear modulus for the 1st and 2nd experiment (Figs. 6-4 (c) and (f)) also increase as the response shown in Fig. 6-2 (e) during fibrillation. However, the shear modulus in the third experiment (Fig.6-3 (h))

didn't increase as the others. Fortunately, the variation in thickness was acceptable, and as mentioned above, the unchanged average shear modulus and viscosity with decrease in the thickness indicate increase in the averaged stiffness of the overall aggregates. The sudden decrease in thickness comparing to the response right before the frequency ramp may also consider as one of the critical point when evaluating Aβ aggregation. Note that there are two frequency ramps in experiment shown in Figs. 6-3 (b) and (c), which is acceptable of possibility of multiple fibril growing stage because the fibrillation is characterized in stepwise dynamic [106-108].

Since the fibril growing interval is confirmed to vary among experiments (Fig. 5-5, Fig. 5-8, Fig. 6-3, and Fig. 6-6), we decide to analyze the viscoelastic response under stage-dependence according to the individual cases. Fig. 6-5 provides a thorough look of all experiments by indicating difference rate (in %) for viscoelastic parameters during the long lag stage and the fibril growing stage from viscoelastic calculations over the overtone experiments. In this figure, two indexes in viscoelastic response are found important in describing the fibril transition because the difference is obvious and without any overlapping in the deviation errors for different stages. First is the decrease rate of thickness from lag stage to fibril stage, which is about 6~-1.5% during the lag

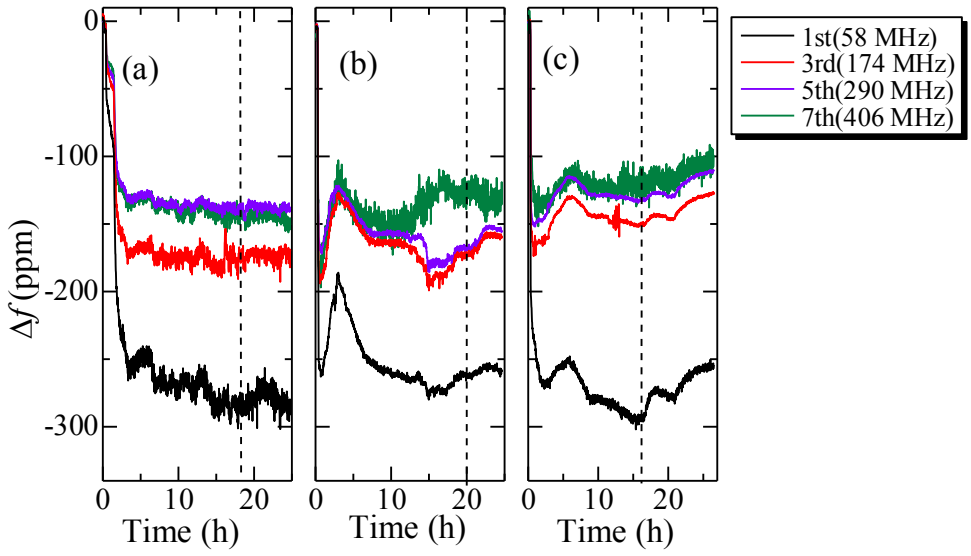

Fig. 6-3 Three independent overtone experiments are shown in (a), (b), and (c), which shows the significant decrease at the arrival of the monomer solution (<~ 1 h), lag stage (until 15~20 h), and the frequency ramps are denoted in vertical dash-lines. Although the amount of the frequency change and the time at the ramp vary from experiments, depending on the initial immobilization condition, *i.e.* distribution, for the seeding materials on the chip, these trends are commonly observed.

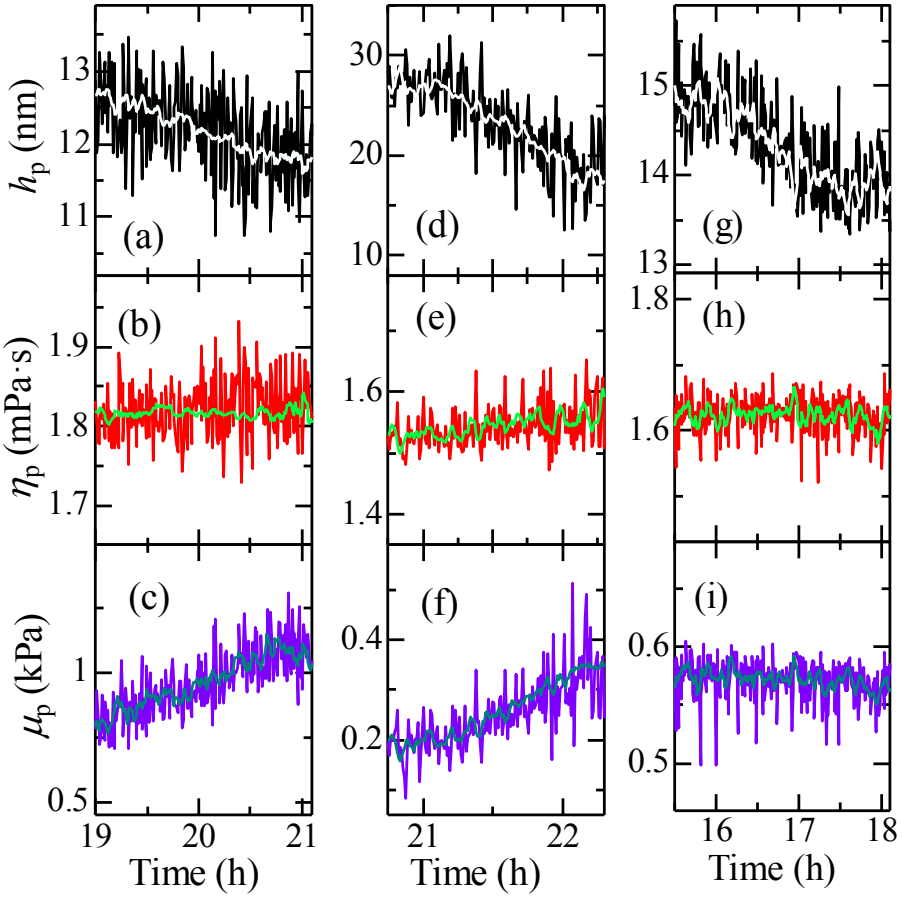

Fig. 6-4 Viscoelastic calculation at the frequency ramp (where the transition to fibril was concerned) of the three independent experiments shown in Fig. 6-3. Result (a, b, c) are thickness, viscosity, and shear modulus of the peptide layer from Fig. 6-3 (a), (d, e, f) are from Fig. 6-3 (b), and (g, h, i) are from Fig. 6-3 (c).

stage and dropped to -9~-22% in fibril growing stage. Another is the increase rate of shear stiffness, which reaches a maximum of about 75% for increment in fibril growing stage while the increase rate is only -2~1% during lag stage. Without any overlapping in deviation errors in the increase rate, the thickness and shear stiffness are proven again to be the important sign of the fibril growing stage of Aβ oligomers transformation into fibrils. The gradual decrease in viscosity was also observable though the average, but it would become unacceptable when cases where the viscosity lies in the range of about -1.5~-7%.

On the other hand, a total of three independent correlation experiment results were presented as in Fig. 6-6. For experiment in 6-5 (a), the experiment stopped at 15.5 h with relative AFM image shown in Fig. 6-6 (d). In this image, only a huge crystal-like amorphous structure, about 2 μm, was observed, without any fibril. For experiment in Figs. 6-6 (b) and (c), which are two experiments stopped after the frequency ramp (26

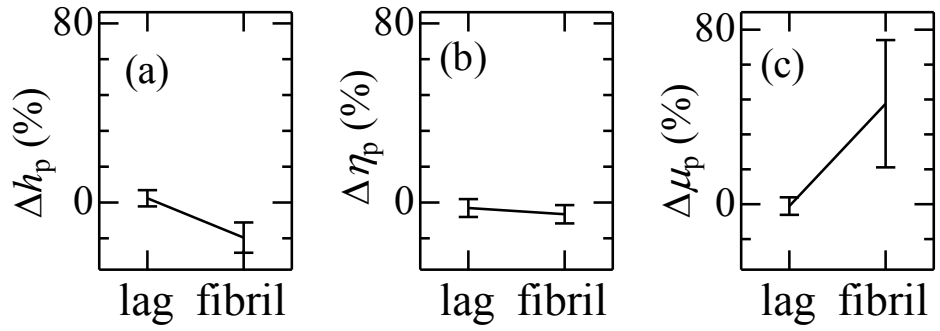

Fig. 6-5 The averaged difference rate ((*b'*-*b*)/*b*) in viscoelasticity, where *b* = (a) peptide thickness, (b) viscosity, and (c) shear stiffness in percentage (%), of Aβ transition from lag stage to fibril growing stage for all data are from the viscoelastic calculation of overtone experiments (Fig 6-2 and Fig. 6-4). *Note that the data used for lag stage were the viscoelastic response from 5 to 10 h for all experiment due to the calculated shear modulus of (b) does not converge at the near-end of lag stage (around 14 to 18 h). The interval of fibril growing stage are based on the time interval in 18 to 20 h for Fig. 6-2, 19 to 21 h for Fig 6-3 (a), 21 to 22 h for Fig 6-3 (b), 16 to 17.7 h for Fig 6-3 (c).

h and 23.5 h). The relative QCM surface was also covered with fibrils in AFM images (Figs. 6-6 (e), (f), and (g)) as in Fig. 5-8 (g) and Fig. 5-9. These plots and AFM images again strengthen the assumption of the correlation between frequency ramp in QCM frequency response to fibrillation of Aβ peptide on QCM surface.

Though it has been verified by the correlation experiment that the frequency ramps should be the transition, the shear modulus in experiment three (Fig. 6-3 (c)) did not respond to the surface structure transition apparently (Fig 6-3 (i)). This may be because of two reasons. First is the initial condition in making $A\beta_{1\text{-}42}$ seed, since only partial of the seed solution was checked by ThT fluorescence, the characteristic of $A\beta_{1\text{-}42}$ seed bulk solution was possible of unidentical. Second is initial seeds immobilization, due to $A\beta_{1\text{-}42}$ seeds were immobilized non-specifically in our experiments, the initial of the QCM surface would vary and would cause different numbers of $A\beta_{1\text{-}40}$ monomer to be trapped by seeds because of the affinity between $A\beta_{1\text{-}40}$ monomers and $A\beta_{1\text{-}42}$ seeds. Therefore, the quality and quantity of monomers and seeds on quartz surface could random among experiments.

For fibrillation, there were also two uncertainties. First, the stiffness of fibrillation depends strongly on the accumulated monomers on to the seed. Since the viscoelastic model in this study interpreted a homogeneity peptide layer, the fraction of total Aβ peptides to carrier solution (ultrapure water) would affect the averaged viscoelastic

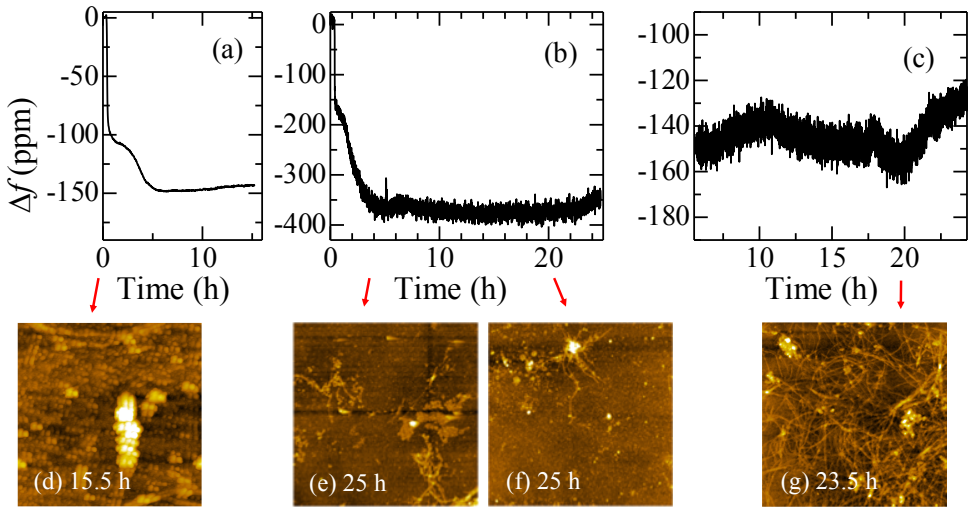

Fig. 6-6 Three independent correlation experiments where (a) is the experiment stopped before the frequency ramp at 15.5 h with (d) cloud-like aggregates in AFM image. (b) and (c) are two experiments stopped at 25 h and 24 h. (e), (f) are the AFM image for (b) and (g) is the AFM image for (c) where AFM image (e), (f), and (g) are found covered with fibrils. All AFM images are in same scale of 5 μm x 5 μm.

parameters of the peptide and solution layer. Next, the fibril orientation is random in this experiment, which would seriously vary the result of forming the cross-fibril network on extreme cases, such as the cases where fibrils aligned in parallel. These could be the main causes of the large deviation error in thickness and stiffness during fibril growing stage as shown in Figs. 6-5 (a) and (c).

Chapter 7. Conclusion and Future Prospective

7-1. Conclusion

Here I would like to conclude the achievement of this work:

1. An Aβ aggregation evaluating system was carried out on the surface of the QCM biosensor by measuring four resonance frequencies (fundamental, 3^{rd}, 5^{th}, 7^{th}) simultaneously and the frequency responses were correlated to conformational change of Aβ aggregation by AFM.
2. The AFM image of the QCM chip surface was taken depending on the characteristic of the QCM frequency responses and three stages are distinguished:
    a. Binding stage: the binding of monomers to seeds, where the resonance frequencies decreased significantly.
    b. Lag stage: incubation before structural transition, where resonance frequencies, especially the fundamental mode, were stable in contrast to the third stage (growing stage).
    c. Fibril growing stage: structural transition from oligomers into fibrils, where resonance frequencies, especially the fundamental mode, had increased greatly.
3. We have succeeded in evaluating the viscoelastic response with only overtone frequencies but without using the dissipation.
4. The viscoelasticity model of Aβ aggregation is successfully established by applying the viscoelastic Voigt model, where we are able to determine Aβ aggregation based on resonance of QCM. The system has proven to be a decisive method for analyzing the aggregation phenomenon.
5. Even though the overall peptide layer was considered homogeneous, where some part of the solution was included, the 3-layer-model was still a predominant tool in evaluating the viscoelastic response during Aβ peptide fibrillation.

7-2. Future Prospective

The viscoelastic model used in this work is greatly simplified, where the layers were regarded as a continuous and homogenous layer despite the fact that the layer includes both the aggregates and the surrounding solution. However, the overall property of the peptide layer was remarkably responded to fibrillation, because Aβ fibril shows great stiffness. The mechanical properties related to the fibril formation can then be evaluated macroscopically. A more appropriate model, which considers the island growth of Aβ aggregates around specifically adsorbed nuclei, will be an interesting development.

The model may be applied in further analysis of other fibrillation characteristics,

such as duration, rate and interval of the fibrillation upon introduction of impurities such as inhibitors and different solvents.

References

[1] A. Burns and S. Iliffe, "Alzheimer's Disease," *BMJ*, **338**, b1589 (2009).

[2] Alzheimer's Disease International: https://www.alz.co.uk/research/statistics

[3] G. M. Shankar and D. M. Walsh, "Alzheimer's Disease: Synaptic Dysfunction and Aβ," *Mol. Neurodegener.*, **4**:48 (2009).

[4] J. R. Harris and F. Fahrenholz, "Subcellular Biochemistry Volume 38: Alzheimer's Disease Cellular and Molecular Aspects of Amyloid β," *Springer US*, 79-103 (2005).

[5] M. F. Mendez, "Early-Onset Alzheimer's Disease: Nonamnestic Subtypes and Type 2 AD," *Arch. Med. Res.*, **43**, 677-685 (2012).

[6] R. L. Nussbaum and C. E. Ellis, "Alzheimer's Disease and Parkinson's Disease," *N. Engl. J. Med.*, **348**, 1356-1364 (2003).

[7] M. Masellis, K. Sherborn, P. R. Neto, D. A. Sadovnick, G.-Y. R. Hsiung, S. E. Black, S. Prasad, M. Williams, and S. Gauthier, "Early-Onset Dementias: Diagnostic and Etiological Considerations," *Alzheimers Res. Ther.*, **5**, S7 (2013).

[8] D. J. Selkoe, "Alzheimer's Disease: Genes, Proteins, and Therapy," *Physiol. Rev.*, **81**, 741-766 (2001).

[9] G. Blessed, B. E. Tomlinson, and M. Roth, "The Association Between Quantitative Measures of Dementia and of Senile Change in the Cerebral Grey Matter of Elderly Subjects," *Br. J. Psychiatry*, **114**, 797-811 (1968).

[10] G. G. Glenner and C. W. Wong, "Alzheimer's Disease: Initial Report of the Purification and Characterization of a Novel Cerebrovascular Amyloid Protein," *Biochem. Biophys. Res. Commun.*, **120**, 885-890 (1984).

[11] G. G. Glenner and C. W. Wong, "Alzheimer's Disease and Down's Syndrome: Sharing of a Unique Cerebrovascular Amyloid Fibril Protein," *Biochem. Biophys. Res. Commun.*, **122**, 1131-1135 (1984).

[12] G. G. Glenner, "Alzheimer's Disease (Senile Dementia): A Research Update and Critique with Recommendations," *J. Am. Geriatr. Soc.*, **30**, 59-62 (1982).

[13] F. M. LaFerla, K. N. Green and S. Oddo, "Intracellular Amyloid-β in Alzheimer's Disease," *Nat. Rev. Neurosci.*, **8**, 499-509 (2007).

[14] J. D. Gillmore and P. N. Hawkins, "Pathophysiology and Treatment of Systemic Amyloidosis," *Nat. Rev. Nephrol.*, **9**, 574-586 (2013).

[15] M. G. Spillantini, M. L. Schmidt, V. M. Lee, J. Q. Trojanowski, R. Jakes, and M. Goedert, "Alpha-Synuclein in Lewy Bodies," *Nature*, **388**, 839-840 (1997).

[16] R. Scarpioni, M. Ricardi, V. Albertazzi, S. De Amicis, F. Rastelli, and L. Zerbini, "Dialysis-Related Amyloidosis: Challenges and Solutions," *Int. J. Nephrol. Renovasc. Dis.*, **9**, 319-328 (2016).

[17] S. B. Prusiner, "Prions," Proc. *Natl. Acad. Sci. U. S. A.*, **95**, 13363-13383 (1998).

[18] P. McColgan, S. J. Tabrizi, “Huntington's Disease: A Clinical Review,” *Eur. J. Neurol.*, **25**, 24-34 (2018).

[19] R. E. Speight and M. A. Cooper, “A Survey of the 2010 Quartz Crystal Microbalance Literature,” *J. Mol. Recognit.*, **25**, 451-473 (2012).

[20] S. Vigneshvar, C. C. Sudhakumari, B. Senthilkumaran, and H. Prakash, “Recent Advances in Biosensor Technology for Potential Applications - An Overview,” *Front. Bioeng. Biotechnol.*, **4**:11 (2016).

[21] S. Katzir "Who Knew Piezoelectricity? Rutherford and Langevin on Submarine Detection and the Invention of Sonar," *Notes Rec. R. Soc.*, **66**, 141–157. (2012)

[22] G. Z. Sauerbrey, “Use of Quartz Vibration for Weighing Thin Films on a Microbalance,” *Physik Journal*, **155**, 206-212 (1959).

[23] A. P. Abbott, J. Griffith, S. Nandhra, C. O'Connor, S. Postlethwaite, K. S. Ryder, and E. L. Smith, “Sustained Electroless Deposition of Metallic Silver from a Choline Chloride-Based Ionic Liquid,” *Surf. Coat. Technol.*, **202**, 2033-2039 (2008).

[24] F. Pena-Pereira, R. M. B. O. Duarte, and A. C. Duarte, “Immobilization Strategies and Analytical Applications for Metallic and Metal-Oxide Nanomaterials on Surfaces,” *Trends Anal. Chem.*, **40**, 90-105 (2012).

[25] K. K. Kanazawa and J. G. Gordon II, “Frequency of a Quartz Microbalance in Contact with Liquid,” *Anal. Chem.*, **57**, 1770-1771 (1985).

[26] K. K. Kanazawa and J. G. Gordon II “The Oscillation Frequency of a Quartz Resonator in Contact with a Liquid,” *Anal. Chim. Acta*, **175**, 99-105 (1985).

[27] U. Reischl, “Molecular Diagnosis of Infectious Diseases,” *Humana Press*, **13**, 519-529 (1998).

[28] K. A. Marx, “Quartz Crystal Microbalance: A Useful Tool for Studying Thin Polymer Films and Complex Biomolecular Systems at the Solution-Surface Interface,” *Biomacromolecules*, **4**, 1099-1119 (2003).

[29] M. Thompson, A. L. Kipling, W. C. Duncan-Hewitt, L. V. Rajaković, and B. A. Čavić-Vlasak, “Thickness-Shear-Mode Acoustic Wave Sensors in the Liquid Phase. a Review,” *Analyst*, **116**, 881-890 (1991).

[30] R. Lucklum, S. Schranz, C. Behling, F. Eichelbaum, and P. Hauptmann, “Analysis of Compressional-Wave Influence on Thickness-Shear-Mode Resonators in Liquids,” *Sens. Actuators A Phys.*, **60**, 40-48 (1997).

[31] W. H. King, “Piezoelectric Sorption Detector,” *Anal. Chem.*, **36**, 1735-1739 (1964).

[32] K. Bodenhöfer, A. Hierlemann, G. Noetzel, U. Weimar, and W. Göpel, “Performances of Mass-Sensitive Devices for Gas Sensing: Thickness Shear Mode and Surface Acoustic Wave Transducers,” *Anal. Chem.,* **68**, 2210-2218 (1996).

[33] J. Zhang, J. Q. Hu, F. R. Zhu, H. Gong, and S. J. O’Shea, “Quartz Crystal Microbalance Coated with Sol-Gel-Derived Thin Films as Gas Sensor for NO Detection,” *Colloids Surf.*

A Physicochem. Eng. Asp., **236**, 23-30 (2004).

[34] M. Penza, P. Aversa, G. Cassano, D. Suriano, W. Wlodarski, M. Benetti, D. Cannatà, F. D. Pietrantonio, and E. Verona, "Thin-Film Bulk-Acoustic-Resonator Gas Sensor Functionalized with a Nanocomposite Langmuir–Blodgett Layer of Carbon Nanotubes," *IEEE Trans. Electron. Devices*, **55**, 1237-1243 (2008).

[35] M. C. Dixon, "Quartz Crystal Microbalance with Dissipation Monitoring: Enabling Real-Time Characterization of Biological Materials and Their Interactions," *J. Biomol. Tech.*, **19**, 151-158 (2008).

[36] Q. Chena, S. Xua, Q. Liu, J. Masliyah, and Z. Xu, "QCM-D Study of Nanoparticle Interactions," *Adv. Colloid Interface Sci.*, **233**, 94-114 (2016).

[37] B. K. Sinha and D. S. Stevens, "Thickness-Shear Vibrations of a Beveled At-Cut Quartz Plate," *J. Acoust. Soc. Am.*, **66**, 192-196 (1979).

[38] L. Li, M. Esashi, and T. Abe, "A Miniaturized Biconvex Quartz-Crystal Microbalance with Large-Radius Spherical Thickness Distribution," *Appl. Phys. Lett.*, **85**, 2652 (2004).

[39] U. Hempel, R. Lucklum, P. R. Hauptmann, E. P. EerNisse, D. Puccio, and R. F. Diaz, "Quartz Crystal Resonator Sensors Under Lateral Field Excitation-A Theoretical and Experimental Analysis," *Meas. Sci. Technol.*, **19**, 055201 (2008).

[40] Y.-Y. Chen, Y.-T. Lai, and C.-H. Hsu, "Investigation of Pseudo Lateral Field Excited Acoustic Wave Gas Sensors with Finite Element Method," *Jpn. J. Appl. Phys.*, **53**, 07KD01 (2014).

[41] H. Ogi, K. Motoshisa, T. Matsumoto, K. Hatanaka, and M. Hirao, "Isolated Electrodeless High-Frequency Quartz Crystal Microbalance for Immunosensors," *Anal. Chem.*, **78**, 6903-6909 (2006).

[42] F. Kato, H. Ogi, T. Yanagida, S. Nishikawa, M. Nishiyama, M. Hirao, "High-Frequency Electrodeless Quartz Crystal Microbalance Chip with a Bare Quartz Resonator Encapsulated in a Silicon Microchannel," *Jpn. J. Appl. Phys.*, **50**, 07HD03 (2011).

[43] H. Ogi, "Wireless-Electrodeless Quartz-Crystal-Microbalance Biosensors for Studying Interactions Among Biomolecules: A Review," *Proc. Jpn. Acad. Ser. B*, **89**, 401-417 (2013).

[44] K. S. McKeating, A. Aubé, and J.-F. Masson, "Biosensors and Nanobiosensors for Therapeutic Drug and Response Monitoring," *Analyst*, **141**, 429-449 (2016).

[45] S. Song, H. Xu, and C. Fan, "Potential Diagnostic Applications of Biosensors: Current and Future Directions," *Int. J. Nanomed.*, **1**, 433-440 (2006).

[46] P. Wang, G. Xu, L. Qin, Y. Xu, Y. Li, and R. Li, "Cell-Based Biosensors and Its Application in Biomedicine," *Sens. Actuators B Chem.*, **108**, 576-584 (2005).

[47] A. Amine, H, Mohammadi, I. Bourais, and G. Palleschi, "Enzyme Inhibition-Based Biosensors for Food Safety and Environmental Monitoring," *Biosens. Bioelectron.*, **21**, 1405-1423 (2006).

[48] L. C. Clark, Jr. and C. Lyons, "Electrode Systems for Continuous Monitoring in Cardiovascular Surgery," *Ann. N Y Acad. Sci.*, **102**, 29-45 (1962).

[49] F. Hafner, "Cytosensor® Microphysiometer: Technology and Recent Applications," *Biosens. Bioelectron.*, **15**, 149-158 (2000).

[50] K. W. Dunn, S. Mayor, J. N. Myers, and F. R. Maxfield, "Applications of Ratio Fluorescence Microscopy in the Study of Cell Physiology," *FASEB J.*, **8**, 573-582 (1994).

[51] H. H. Nguyen, J. Park, S. Kang, and M. Kim, "Surface Plasmon Resonance: A Versatile Technique for Biosensor Applications," *Sensors (Basel)*, **15**, 10481-10510 (2015).

[52] T. Nomura and M. Okuhara, "Frequency Shifts of Piezoelectric Quartz Crystals Immersed in Organic Liquids," *Anal. Chim. Acta*, **142**, 281-284 (1982).

[53] S. Kurosawa, E. Tawara, N. Kamo, Y. Kobatake "Oscillating Frequency of Piezoelectric Quartz Crystal in Solutions," *Anal. Chim. Acta*, **230**, 41-49 (1990).

[54] H. Ogi, H. Nagai, Y. Fukunishi, M. Hirao, and M. Nishiyama, "170-MHz Electrodeless Quartz Crystal Microbalance Biosensor: Capability and Limitation of Higher Frequency Measurement," *Anal. Chem.*, **81**, 8068-8073 (2009).

[55] H. Ogi, K. Motohisa, K. Hatanaka, T. Ohmori, M. Hirao, and M. Nishiyama, "Concentration Dependence of IgG-Protein A Affinity Studied by Wireless-Electrodeless QCM," *Biosens. Bioelectron.*, **22**, 3238-3242. (2007)

[56] F. Langer, Y. S. Eisele, S. K. Fritschi, M. Staufenbiel, L. C. Walker, and M. Jucker, "Soluble Aβ Seeds Are Potent Inducers of Cerebral β-Amyloid Deposition," *J. Neurosci.*, **31**, 14488-14495 (2011).

[57] M. R. Nilssonm, "Techniques to Study Amyloid Fibril Formation in Vitro," *Methods*, **34**, 151-160 (2004).

[58] C. Soto, E. M. Sigurdsson, L. Morelli, R. A. Kumar, E. M. Castaño, and B. Frangione, "β-Sheet Breaker Peptides Inhibit Fibrillogenesis in a Rat Brain Model of Amyloidosis: Implication for Alzheimer's Therapy," *Nat. Med.*, **4**, 822-826 (1998).

[59] H. Ogi, Y. Fukunishi, T. Yanagida, H. Yagi, Y. Goto, M. Fukushima, K. Uesugi, and M. Hirao, "Seed-Dependent Deposition Behavior of Aβ Peptides Studied with Wireless Quartz-Crystal-Microbalance Biosensor," *Anal. Chem.*, **83**, 4982-4988 (2011).

[60] H. Ogi, M. Fukukshima, H. Hamada, K. Noi, M. Hirao, H. Yagi, and Y. Goto, "Ultrafast Propagation of β-Amyloid Fibrils in Oligomeric Cloud," *Sci. Rep.*, **4**, 6960. (2014)

[61] T. Iwatsubo, A. Odaka, N. Suzuki, H. Mizusawa, N. Nukina, and Y. Ihara, "Visualization of Aβ42(43) and Aβ40 in Senile Plaques with End-Specific Aβ Monoclonals: Evidence That an Initially Deposited Species is Aβ42(43)," *Neuron*, **13**, 45-53 (1994).

[62] S. A. Gravina, L. B. Ho, C. B. Eckman, K. E. Long, L. Otvos Jr., L. H. Younkin, N. Suzuki, and S. G. Younkin, "Amyloid β Protein (Aβ) in Alzheimer's Disease Brain," *J. Biol. Chem.*, **270**, 7013-7016 (1995).

[63] J. T. Jarrett, E. P. Berger, and P. T. Lansbury Jr., "The Carboxy Terminus of the β Amyloid

Protein Is Critical for the Seeding of Amyloid Formation: Implications for the Pathogenesis of Alzheimer's Disease," *Biochemistry*, **32**, 4693-4697 (1993).

[64] N. Suzuki, T. T. Cheung, X. D. Cai, A. Odaka, L. Otvos Jr, C. Eckman, T. E. Golde, and S. G. Younkin, "An Increased Percentage of Long Amyloid Beta Protein Secreted by Familial Amyloid Beta Protein Precursor (beta APP717) Mutants," *Science*, **264**, 1336-1340. (1994)

[65] S. Vivekanandan, J. R. Brender, S. Y. Lee, and A. Ramamoorthy, "A Partially Folded Structure of Amyloid-Beta (1-40) in an Aqueous Environment," *Biochem. Biophys. Res. Commun.*, **411**, 312-316 (2011).

[66] M. Bucciantini, E. Giannoni, F. Chiti, F. Baroni, L. Formigli, J. Zurdo, N. Taddei, G. Ramponi, C. M. Dobson, and M. Stefani, "Inherent Toxicity of Aggregates Implies a Common Mechanism for Protein Misfolding Diseases," *Nature*, **416**, 507-511 (2002).

[67] I. Daigle and C. Li, "Apl-1, a Caenorhabditis Elegans Gene Encoding a Protein Related to the Human Beta-Amyloid Protein Precursor," *Proc. Natl. Acad. Sci. U.S.A.*, **90**, 12045-12049 (1993).

[68] E. Kojro and F. Fahrenholz, "The Non-Amyloidosis Pathway: Structure and Function of Alpha-Secretases," *Subcell. Biochem.*, **38**, 105-127 (2005).

[69] R. Vassar, B. D. Bennett, S. Babu-Khan, S. Kahn, E. A. Mendiaz, P. Denis, D. B. Teplow, S. Ross, P. Amarante, R. Loeloff, Y. Luo, S. Fisher, J. Fuller, S. Edenson, J. Lile, M. A. Jarosinski, A. L. Biere, E. Curran, T. Burgess, J.-C. Louis, F. Collins, J. Treanor, G. Rogers, and M. Citron, "β-Secretase Cleavage of Alzheimer's Amyloid Precursor Protein by the Transmembrane Aspartic Protease BACE," *Science*, **286**, 735-741 (1999).

[70] P. D. Mehta, T. Pirttilä, S. P. Mehta, E. A. Sersen, P. S. Aisen, and H. M. Wisniewski, "Plasma and Cerebrospinal Fluid Levels of Amyloid β Proteins 1-40 and 1-42 in Alzheimer Disease," *Arch. Neurol.*, **57**, 100-105 (2000).

[71] S. Y. Fung, C. Keyes, J. Duhamel, and P. Chen, "Concertation Effect on the Aggregation of a Self-Assembling Oligopeptide," *Biophys. J.*, **85**, 537-548 (2003).

[72] A. Parbhu, H. Lin, J. Thimm, R. Lal, "Imaging Real-Time Aggregation of Amyloid Beta Protein (1-42) by Atomic Force Microscopy," *Peptides*, **23**, 1265-1270 (2002).

[73] T. Lührs, C. Ritter, M. Adrian, D. Riek-Loher, B. Bohrmann, H. Döbeli, D. Schubert, R. Riek, "3D Structure of Alzheimer's Amyloid-β (1-42) Fibrils," *Proc. Natl. Acad. Sci. U.S.A.*, **102**, 17342-17347 (2005).

[74] M. P. Lambert, A. K. Barlow, B. A. Chromy, C. Edwards, R. Freed, M. Liosatos, T. E. Morgan, I. Rozovsky, B. Trommer, K. L. Viola, P. Wals, C. Zhang, C. E. Finch, G. A. Krafft, and W. L. Klein, "Diffusible, Nonfibrillar Ligands Derived from $A\beta_{1\text{-}42}$ are Potent Central Nervous System Neurotoxins," *Proc. Natl. Acad. Sci. U.S.A.*, **95**, 6448-6453 (1998).

[75] A. T. Petkova, R. D. Leapman, Z. Guo, W.-M. Yau, M. P. Mattson, and R. Tycko, "Self-

Propagating, Molecular-Level Polymorphism in Alzheimer's β-Amyloid Fibrils," *Science*, **307**, 262-265 (2005).

[76] W. Qiang, W.-M. Yau, J.-X. Lu, J. Collinge, and R. Tycko, "Structural Variation in Amyloid-β Fibrils from Alzheimer's Disease Clinical Subtypes," *Nature*, **541**, 217-221 (2017).

[77] J. A. Kotarek, K. C. Johnson, M. A. Moss, "Quartz Crystal Microbalance Analysis of Growth Kinetics for Aggregation Intermediates of the Amyloid-β Protein," *Anal. Biochem.*, **378**, 15-24 (2008).

[78] T. P. J. Knowles, W. Shu, G. L. Devlin, S. Meehan, S. Auer, C. M. Dobson, and M. E. Welland, "Kinetics and Thermodynamics of Amyloid Formation from Direct Measurements of Fluctuations in Fibril Mass," *Proc. Natl. Acad. Sci. U.S.A.*, **104**, 10016-10021 (2007).

[79] Y.-K. Yong, J. T. Stewart, J. Detaint, A. Zarka, B. Capelle, and Y. Zheng, "Thickness-Shear Mode Shapes and Mass-Frequency Influence Surface of a Circular and Electroded AT-Cut Quartz Resonator," *IEEE Trans. Ultrason. Ferroelectr. Freq. Control*, **39**, 609-617 (1992).

[80] P. C. Y. Lee and Y. K. Yong, "Frequency-Temperature Behavior of Thickness Vibrations of Doubly Rotated Quartz Plates Affected by Plate Dimensions and Orientations," *J. Appl. Phys.*, **60**, 2327-2342 (1986).

[81] W. J. Spence, "Transverse Thickness Modes in BT-Cut Quartz Plates," *J. Acoust. Soc. Am.*, **41**, 994-1001 (1967).

[82] K. K. Zadeh, A. Trinchi, W. Wlodarski, and A. Holland, "A Novel Love-Mode Device Based on a ZnO/ST-Cut Quartz Crystal Structure for Sensing Application," *Sens. Actuators A Phys.*, **100**, 135-143 (2002).

[83] H. Ogi, H. Nagai, Y. Fukunishi, T Yanagida, M. Hirao, and M Nishiyama, "Multichannel Wireless-Electrodeless Quartz-Crystal Microbalance Immunosensor," *Anal. Chem.*, **82**, 3957-3962 (2010).

[84] H. Hamada, H. Ogi, K. Noi, H. Yagi, Y. Goto, and M. Hirao, "Nucleation-Fibrillation Dynamics of Aβ1-40 Peptides on Liquid–solid Surface Studied by Total-Internal-Reflection Fluorescence Microscopy Coupled with Quartz-Crystal Microbalance Biosensor," *Jpn. J. Appl. Phys.*, **54**, 07HE01 (2015).

[85] H. Ogi, Y. Fukunishi, H. Nagai, K. Okamoto, M. Hirao, and M. Nishiyama, "Nonspecific-Adsorption Behavior of Polyethylenglycol and Bovine Serum Albumin Studied by 55-MHz Wireless-Electrodeless Quartz Crystal Microbalance," *Biosens. Bioelectron.*, **24**, 3148-3152 (2009).

[86] T. Shagawa, H. Torii, F. Kato, H. Ogi, and M. Hirao, "Viscoelasticity Evolution in Protein Layers During Binding Reactions Evaluated Using High-Frequency Wireless and Electrodeless Quartz Crystal Microbalance Biosensor Without Dissipation," *Jpn. J. Appl.*

Phys., **54**, 096601 (2015).

[87] T. Shagawa, H. Torii, F. Kato, H. Ogi, and M. Hirao, "Relationship Between Viscosity Change and Specificity in Protein Binding Reaction Studied by High-Frequency Wireless and Electrodeless MEMS Biosensor," *Jpn. J. Appl. Phys.*, **54**, 068001 (2015).

[88] D. S. Bailey, M. M. Driscoll, R. A. Jelen, B. R. McAvoy "Frequency Stability of High-Overtone Bulk-Acoustic Resonators," *IEEE Trans. Ultrason. Ferroelectr. Freq. Control*, **39**, 780-784 (1992).

[89] M, A, Meyers and K. K. Chawla, "Mechanical Behavior of Materials," *Cambridge University Press*, 120-126 (2009).

[90] A. Hernández-Jiménez, J. Hernández-Santiago, A. Macias-García, and J. Sánchez-González, "Relaxation Modulus in PMMA and PTFE Fitting by Fractional Maxwell Model," *Polym. Test*, **21**, 325-331 (2002).

[91] A. Tsortos, G. Papadakis, and E. Gizeli, "Shear Acoustic Wave Biosensor for Detecting DNA Intrinsic Viscosity and Conformation: A Study with QCM-D," *Biosens. Bioelectron.*, **24**, 836-841 (2008).

[92] S. X. Liu and J.-T. Kim, "Application of Kelvin-Voigt Model in Quantifying Whey Protein Adsorption on Polyethersulfone Using QCM-D," *J. Lab Autom.*, **14**, 213-220 (2009).

[93] C. E. Reed, K. K. Kanazawa, and J. H. Kaufman, "Physical Description of a Viscoelastically Loaded AT-Cut Quartz Resonator," *J. Appl. Phys.*, **68**, 1993-2001 (1990).

[94] M. Rodahl, F. Höök, A. Krozer, P. Brzezinski, and B. Kasemo, "Quartz Crystal Microbalance Setup for Frequency and Q-Factor Measurements in Gaseous and Liquid Environments," *Rev. Sci. Instrum.*, **66**, 3924-3930. (1995).

[95] M. Rodahl and B. Kasemo, "On the Measurement of Thin Liquid Overlayers with the Quartz-Crystal Microbalance," *Sens. Actuators A Phys.*, **54**, 448-456 (1996).

[96] F. Höök, B. Kasemo, T. Nylander, C. Fant, K. Sott, and H. Elwing, "Variations in Coupled Water, Viscoelastic Properties, and Film Thickness of a Mefp-1 Protein Film during Adsorption and Cross-Linking: A Quartz Crystal Microbalance with Dissipation Monitoring, Ellipsometry, and Surface Plasmon Resonance Study," *Anal. Chem.*, **73**, 5796-5804 (2001).

[97] M. V. Voinova, M. Jonson, and B. Kasemo, "'Missing mass' Effect in Biosensor's QCM Applications," *Biosens. Bioelectron.*, **17**, 835-841 (2002).

[98] M. V. Voinova, M. Jonson, and B. Kasemo, "Dynamics of Viscous Amphiphilic Films Supported by Elastic Solid Substrates," *J. Phys. Condens. Matter*, **9**, 7799-7808 (1997).

[99] M. V. Voinova, M. Rodahl, M. Jonson, and B. Kasemo, "Viscoelastic Acoustic Resonance of Layered Polymer Films at Fluid-Solid Interface Continuum Mechanics Approach," *Phys. Scr.*, **59**, 391-396 (1999).

[100] A. R. Patel, K. K. Kanazawa, and C. W. Frank, "Antibody Binding to a Tethered

Vesicle Assembly Using QCM-D," *Anal. Chem.*, **81**, 6021-6029 (2009).

[101] M. Yan, C. Liu, D. Wang, J. Ni, and J. Cheng, "Characterization of Adsorption of Humic Acid onto Alumina using Quartz Crystal Microbalance with Dissipation," *Langmuir*, **27**, 9860-9865 (2011).

[102] N. B. Eisele, F. I. Andersson, S. Frey, and R. P. Richter, "Viscoelasticity of Thin Biomolecular Films: A Case Study on Nucleoporin Phenylalanine-Glycine Repeats Grafted to a Histidine-Tag Capturing QCM-D Sensor," *Biomacromolecules*, **13**, 2322-2332 (2012).

[103] H. Ogi, T. Ohmori, N. Nakamura, and M. Hirao, "Elastic, Anelastic, and Piezoelectric Coefficients of α-Quartz Determined by Resonance Ultrasound Spectroscopy," *J. Appl. Phys.*, **100**, 053511 (2006).

[104] K. Nakajima, H. Ogi, K. Adachi, K. Noi, M. Hirao, H. Yagi, and Y. Goto, "Nucleus Factory on Cavitation Bubble for Amyloid β Fibril," *Sci. Rep.*, **6**, 22015 (2016).

[105] J. F. Smith, T. P. J. Knowles, C. M. Dobson, C. E. MacPhee, and M. E. Welland, "Characterization of the Nanoscale Properties of Individual Amyloid Fibrils," *Proc. Natl. Acad. Sci. U.S.A.*, **103**, 15806-15811 (2006).

[106] T. Ban, M. Hoshino, S. Takahashi, D. Hamada, K. Hasegawa, H. Naiki, and Y. Goto, "Direct Observation of Aβ Amyloid Fibril Growth and Inhibition," *J. Mol. Biol.*, **344**, 757-767 (2004).

[107] M. S. Z. Kellermayer, A. Karsai, M. Benke, K. Soós, and B. Penke, "Stepwise Dynamics of Epitaxially Growing Single Amyloid Fibrils," *Proc. Natl. Acad. Sci. U.S.A.*, **105**, 141-144 (2008).

[108] J. Ferkinghoff-Borg, J. Fonslet, C. B. Andersen, S. Krishna, S. Pigolotti, H. Yagi, Y. Goto, D. Otzen, and M. H. Jensen, "Stop-And-Go Kinetics in Amyloid Fibrillation," *Phys. Rev. E Stat. Nonlin. Soft Matter. Phys.*, **82**, 010901 (2010).

Acknowledgement

Firstly, I would like to express my sincere gratitude to Prof. Hirotsugu Ogi and Prof. Ryuichi Tarumi for the support of my Ph.D. study and related research, for their patience, motivation, and immense knowledge, which helped me throughout the research and writing of this thesis. I could not have imagined having a better professor in advising and mentor for my Ph.D. study.

I would like to thank my former supervisor, Prof. Masahiko Hirao, not only for his insightful comments and encouragement for my research in Graduate school of Engineering Science, but also for leading me into the Solid Mechanics Group.

Besides my advisors, I would like to thank the other committee members for screening this thesis, Prof. Hidetoshi Kobayashi and Prof. Masao Tanaka, not only for their insightful comments, but also for the hard questions that strengthen this thesis.

My sincere thanks also go to Assist. Prof. Nobutomo Nakamura and Dr. Kentaro Noi, who provided me great prospects, and who gave access to the laboratory and research facilities. Without their precious support it would not be possible to conduct this research.

I thank my fellow lab-mates for the decent discussions, for the sleepless nights we were working together before deadlines, and for all the fun we have had in my student life. Also, I thank my friends in the following institution: National Taiwan University and Tatung University in Taiwan. In particular, I am grateful to Prof. Yung-Yu Chen for enlightening me the first glance of research.

Last but not the least, I would like to thank my family: my parents and to my sister for supporting me spiritually throughout writing this thesis and my life in general.

Publication List

1. Yen-Ting Lai, Hirotsugu Ogi, Kentaro Noi, and Fumihito Kato, "Viscoelasticity Response during Fibrillation of Amyloid β Peptides on a Quartz-Crystal-Microbalance Biosensor," Langmuir, 34, 5474-5479 (2018).
2. Yung-Yu Chen, Yen-Ting Lai, and Chao-Hung Hsu, "Investigation of Pseudo Lateral Field Excited Acoustic Wave Gas Sensors with Finite Element Method," *Jpn. J. Appl. Phys.*, **53**, 07KD01 (2014).

Conference Publication

1. Yen-Ting Lai, Hirotsugu Ogi, Arihiro Iwata, and Masahiko Hirao, "Viscoelasticity response during fibrillation of amyloid beta peptides on quartz crystal microbalance biosensor," *Proceedings of Symposium on Ultrasonic Electronics*, **Vol. 37**, 3E2-3 (November 2016).
2. S.Y. Pao, W. Y. Chang, B. Hsu, Y. T. Lai, Y. Y. Chen, T. Lin, and M. K. Chao, "A Study on Raising the Fundamental TS-mode Resistance by Energy Trapping for 3rd Overtone Resonator Performance Enhancement," *2014 IEEE International Frequency Control Symposium*, (July 2014).
3. Yung-Yu Chen and Yen-Ting Lai, "Investigation of Pseudo Lateral Field Excited Acoustic Wave Gas Sensors with Finite Element Method," *Proceedings of the 2013 International Congress on Ultrasonics*, P0185 (May 2013).